

Isostatic constraint for 2D nonlinear gravity inversion on rifted margins

B. Marcela S. Bastos¹ and Vanderlei C. Oliveira Jr.¹

ABSTRACT

We have developed a nonlinear gravity inversion for simultaneously estimating the basement and Moho geometries, as well as the depth of the reference Moho along a profile crossing a passive rifted margin. To obtain stable solutions, we impose smoothness on basement and Moho, force them to be close to previously estimated depths along the profile and also impose local isostatic equilibrium. Different from previous methods, we evaluate the information of local isostatic equilibrium by imposing smoothness on the lithostatic stress exerted at depth. Our method delimits regions that deviate and those that can be considered in local isostatic equilibrium by varying the weight of the isostatic constraint along the profile. It also allows controlling the degree of equilibrium along the profile, so that the interpreter can obtain a set of

candidate models that fit the observed data and exhibit different degrees of isostatic equilibrium. Our method also differs from earlier studies because it attempts to use isostasy for exploring (but not necessarily reducing) the inherent ambiguity of gravity methods. Tests with synthetic data illustrate the effect of our isostatic constraint on the estimated basement and Moho reliefs, especially at regions with pronounced crustal thinning, which are typical of passive volcanic margins. Results obtained by inverting satellite data over the Pelotas Basin, a passive volcanic margin in southern Brazil, agree with previous interpretations obtained independently by combining gravity, magnetic, and seismic data available to the petroleum industry. These results indicate that combined with a priori information, simple isostatic assumptions can be very useful for interpreting gravity data on passive rifted margins.

INTRODUCTION

Gravity methods have long been used to investigate the crustal structure in local studies. A common approach is to approximate the crust by a set of juxtaposed layers with constant or depth-dependent density distributions. The boundaries of these juxtaposed layers are defined by surfaces that generally represent sedimentary layers, bathymetry, relief of basement, or the Mohorovicic discontinuity (the Moho). Here, we consider methods that estimate the geometry of these surfaces. There is a large group of methods estimating the geometry of a single surface representing the basement relief in the space domain (e.g., Bott, 1960; Tanner, 1967; Cordell and Henderson, 1968; Barbosa et al., 1997, 1999a,b; Condi et al., 1999; Silva et al., 2006, 2010, 2014; Chakravarthi and Sundararajan, 2007; Martins et al., 2010, 2011; Lima et al., 2011; Barnes and Barraud, 2012; Silva and Santos, 2017) and the Fourier domain (e.g., Oldenburg, 1974; Granser, 1987; Reamer and Ferguson, 1989; Guspí, 1993). Another group of methods estimate a single surface repre-

senting the Moho in the space domain (e.g., Shin et al., 2009; Bagherbandi and Eshagh, 2012; Barzaghi and Biagi, 2014; Sampietro, 2015; Uieda and Barbosa, 2017) and the Fourier domain (e.g., Braatenberg et al., 1997; Braatenberg and Zadro, 1999; van der Meijde et al., 2013). Finally, there is a small group of methods estimating the geometry of multiple surfaces (e.g., Braatenberg et al., 2003; Camacho et al., 2011; Salem et al., 2014; Ferderer et al., 2017; García-Abdeslem, 2017; Salem, 2017).

All of these methods suffer from the inherent ambiguity (Skeels, 1947; Roy, 1962) in determining the true physical property distribution that produces a discrete set of observed gravity data. It is well-known that, by presuming a fixed density distribution for each layer, it is possible to find different surfaces producing the same gravity data. It is known that methods estimating multiple surfaces suffer from a greater ambiguity if compared with those estimating the geometry of a single surface. This inherent ambiguity is drastically increased for the cases in which, besides the geometry of the surfaces, the density distribution of the layers is also estimated. To

Manuscript received by the Editor 12 November 2018; revised manuscript received 13 September 2019; published ahead of production 18 October 2019; published online 6 December 2019.

¹Observatório Nacional, Department of Geophysics, Rio de Janeiro, Brazil. E-mail: macelabastos@gmail.com; vanderlei@on.br (corresponding author). © 2020 Society of Exploration Geophysicists. All rights reserved.

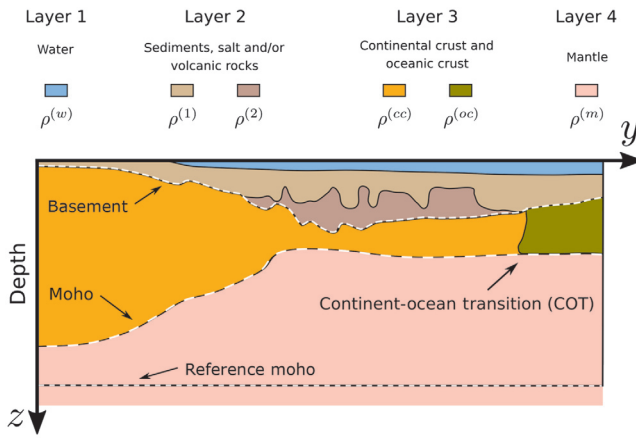


Figure 1. Rifted margin model formed by four layers. Layer 1 represents a water layer with constant density $\rho^{(w)}$. Layer 2 is split into Q sublayers according to the complexity of the study area. In this example, $Q = 2$. These sublayers represent sediments, salt, or volcanic rocks, and they have constant densities of $\rho^{(q)}$, $q = 1, \dots, Q$. Layer 3 represents the crust. In this example, its density $\rho(c)$ assumes two possible values $\rho^{(cc)}$ and $\rho^{(oc)}$ representing, respectively, continental and oceanic crust. More complex models can be generated using a function describing the lateral density variations within the crust. Finally, layer 4 represents a homogeneous mantle with constant density $\rho^{(m)}$. Basement, Moho, and reference Moho are represented by the dashed white lines. The reference mass distribution is formed by an upper layer with constant density $\rho^{(r)}$ and base at the reference Moho. Below this layer, we presume a reference distribution with the same constant density $\rho^{(m)}$ of the mantle.

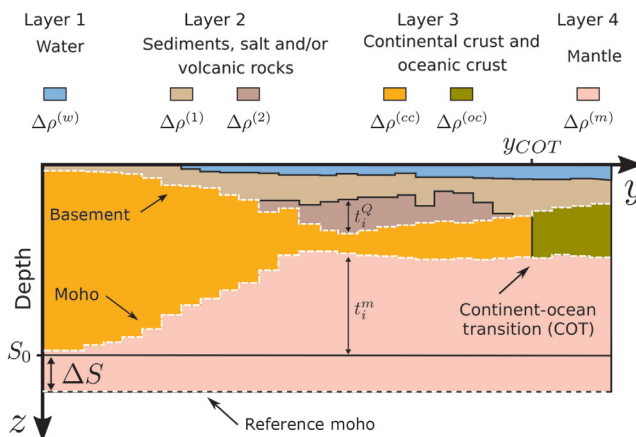


Figure 2. Interpretation model formed by N columns of vertically stacked prisms. Each column is formed by four layers of prisms and locally approximates the rifted margin model shown in Figure 1. Layer 2 is formed by Q sublayers according to the complexity of the study area. In this example, $Q = 2$. The thickness t_i^Q and t_i^m of the prisms forming, respectively, the base of layer 2 and the top of layer 4 at the i th column are indicated. Each prism has a constant density contrast defined as the difference between its corresponding density at the rifted margin model and the constant density $\rho^{(r)}$ of the shallowest layer forming the reference density distribution (Figure 1). Basement, Moho, and the reference Moho are represented by the dashed white lines. The continuous black line represents the compensation depth at S_0 . The reference Moho is located at $S_0 + \Delta S$.

partially overcome the ambiguity and generate meaningful solutions, the interpreter must use a priori information obtained from seismic data and/or boreholes to constrain the range of possible models. Some authors opted for combining gravity data with seismic and isostasy to reduce this inherent ambiguity. As properly pointed out by Gradmann et al. (2017), isostasy is equally sensitive to shallow and deep structures. This characteristic makes it a powerful tool to validate interpretations of deep seismic data and gravity models.

Condi et al. (1999) propose a nonlinear gravity inversion for estimating the offshore deep structures of a rifted margin. Their method uses local isostasy for directly constraining the geometries of the shallow and deeper parts of their model, without necessarily

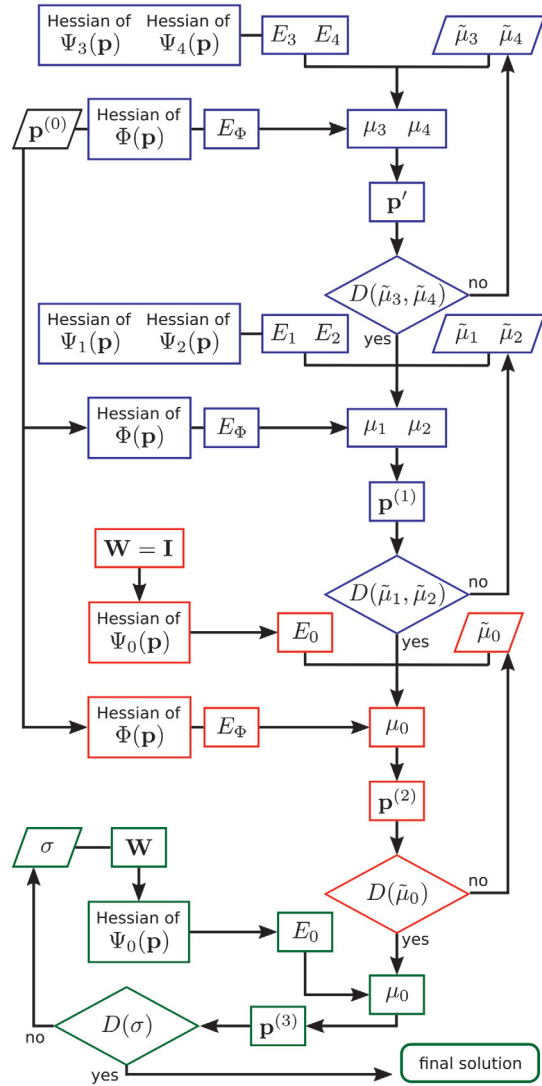


Figure 3. Flow diagram of the algorithm. Steps 1, 2, and 3 are represented in blue, red, and green, respectively. Diamonds, parallelograms, and rectangles represent decision points, input parameters, and intermediary processes, respectively. The end of the algorithm is represented by the rounded rectangle. For convenience, we have omitted some input parameters related to the interpretation model and the inversion (see the “Step 1” subsection). Details about this flow diagram are explained in the “Computational procedures for solving the inverse problem” subsection.

forcing it to be in a perfect isostatic equilibrium. Braitenberg et al. (2003) propose a method for estimating the bathymetry and Moho geometries from gravity data by imposing regional isostatic equilibrium in the frame of a thin-plate isostatic flexure model over an oceanic basin. Salem et al. (2014) present a nonlinear gravity inversion for estimating the surfaces representing the basement and Moho on an onshore rifted basin. The basement relief is estimated using an iterative approach similar to that presented by Bott (1960) and Cordell and Henderson (1968). The difference is that, at each iteration, the Airy-Heiskanen model (Heiskanen and Moritz, 1967, p. 135) for local isostatic equilibrium is used to subsequently update the Moho geometry, forcing the model to be in perfect isostatic equilibrium according to the Airy-Heiskanen model. We note that their method does not estimate the geometries of the basement and Moho simultaneously. As pointed out by Silva et al. (2014), Bott's method does not define optimal step sizes at the iterative corrections, does not impose constraints for obtaining stable solutions, nor does it use an objective stopping criterion. Consequently, the method presented by Salem et al. (2014) is also susceptible to these limitations. García-Abdeslem (2017) uses an approach based on flexural isostasy to estimate the Moho and compute a regional gravity field, which is subsequently subtracted from the observed gravity data to obtain a residual gravity field. His method consists of solving a nonlinear inverse problem for estimating the basement geometry explaining the residual gravity field. Salem (2017) presents a general framework for estimating the surfaces associated with the basement and Moho on a rifted continental margin. His method is based on an empirical logistic function that acts as a gain control of the Moho uplift and introduces information about isostatic equilibrium by correlating the gravity data produced by the basement and Moho. Similar to Salem et al. (2014) and García-Abdeslem (2017), the method presented by Salem (2017) does not estimate the surfaces of the basement and Moho simultaneously. The Moho surface is estimated in a first step and then used to estimate the basement surface. Ferderer et al. (2017) propose a “general local isostasy” approach that consists of combining the Airy-Heiskanen and Pratt-Hayford models (Heiskanen and Moritz, 1967) so that the crust density and geometry may vary laterally to maintain the local isostatic equilibrium on a profile crossing a rifted margin. Their approach also uses local isostasy to directly link the geometries of shallow and deeper structures with the purpose of reducing the range of possible solutions. They propose a method for estimating the geometries of basement and Moho and density contrasts using a grid-search technique (Sen and Stoffa, 2013). Such techniques involve the systematic search for model parameters producing the best data fit and may be far from practical in geophysical

Table 1. Properties of the synthetic margin model with geometry based on the East Greenland margin.

Geologic meaning	$\rho^{(a)}$ (kg/m ³)	$\Delta\rho^{(a)}$ (kg/m ³)	α
Water	1030	-1820	w
Sediments	2600	-250	1
Continental crust	2850	0	cc
Oceanic crust	2885	35	oc
Mantle	3250	400	m

The model extends from $y = 0$ km to $y = 380$ km, the COT is located at $y_{\text{COT}} = 165$ km, and the reference Moho is located at 53 km (Figures 1 and 2). The density contrasts $\Delta\rho^{(a)} = \rho^{(a)} - \rho^{(r)}$ were defined using the reference value $\rho^{(r)} = 2850$ kg/m³, which coincides with the density $\rho^{(cc)}$ attributed to the continental crust.

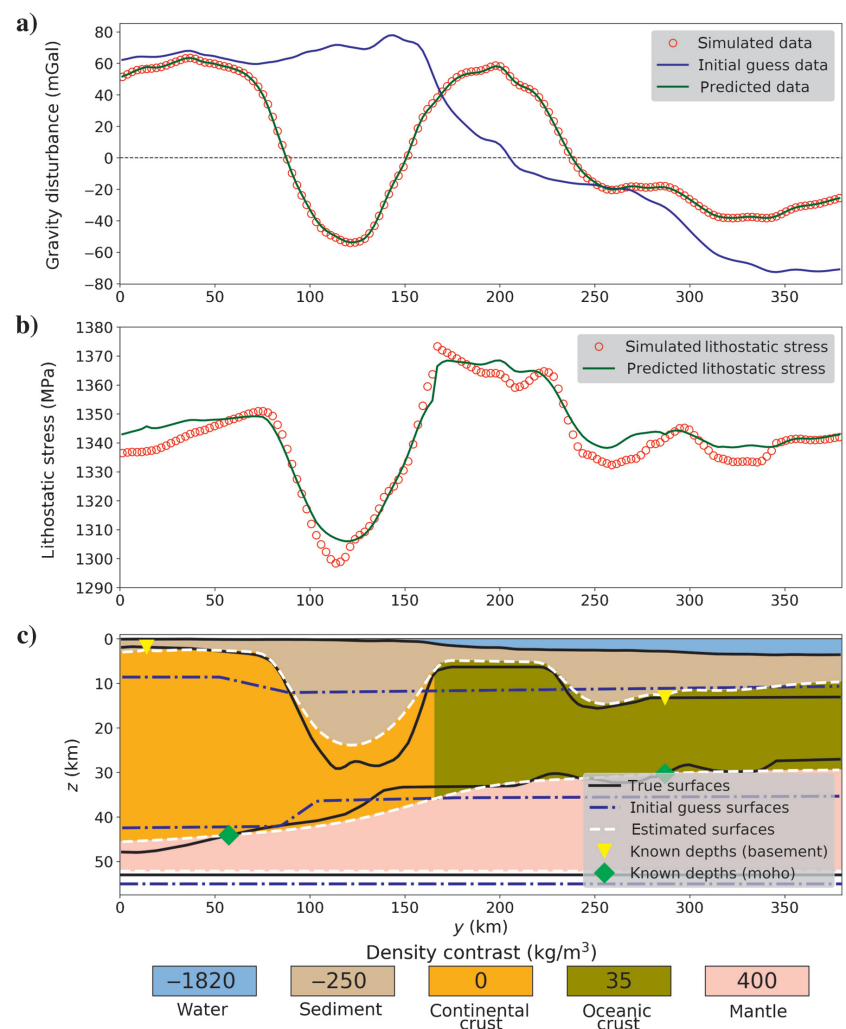


Figure 4. Application to synthetic data produced by the model based on the East Greenland margin. Estimated model $\mathbf{p}^{(1)}$ obtained at the end of step 1 (Figure 3) using $\tilde{\mu}_1 = 10^1$ and $\tilde{\mu}_2 = 10^2$. (c) True and estimated surfaces, initial basement and Moho (initial guess) and a priori information at points on basement and Moho (known depths). (b) True and predicted lithostatic stress curves (equation 9). (a) Gravity disturbance produced by the true model (simulated data), by the estimated model (predicted data), and by the initial guess (initial guess data). The density contrasts are those shown in Table 1 and $S_0 = 48$ km.

applications for cases in which the model space is very large and the forward problem is slow.

We present a nonlinear gravity inversion method for simultaneously estimating the geometries of the basement and Moho, as well as a constant depth representing a reference Moho along a profile crossing a rifted margin. Our method is formulated, in the space domain, as a nonlinear gravity inversion based on the Levenberg-Marquardt method (Silva et al., 2001; Aster et al., 2005), by following the same strategy of Barbosa et al. (1999b) to incorporate inequality constraints. The parameters to be estimated are the constant depth representing the reference Moho and the geometries of the basement and Moho. At each iteration, our method simultaneously estimates corrections for the reference Moho, as well as the geometries of basement and Moho. To produce stable solutions, we use different constraints imposing smoothness on basement and Moho surfaces. In addition, we force them to be close to some depths along the profile.

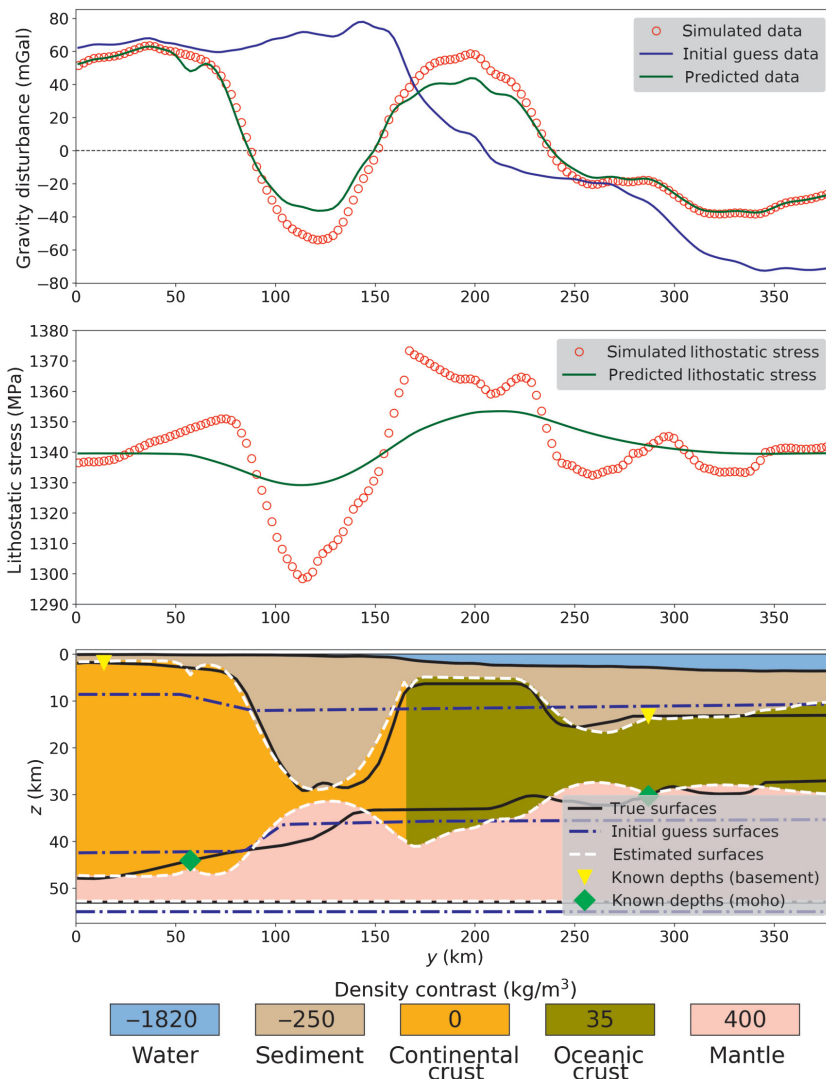


Figure 5. Application to synthetic data produced by the model based on the East Greenland margin. Estimated model $\mathbf{p}^{(2)}$ obtained at the end of step 2 (Figure 3) using $\tilde{\mu}_0 = 10^3$. The remaining information is the same as that shown in the caption of Figure 4.

Similar to Ferderer et al. (2017), we combine the Airy-Heiskanen and Pratt-Hayford models to impose local isostatic equilibrium. However, there are three significant differences between our approach and those presented in earlier studies. The first one is the way we impose isostatic equilibrium. Different from previous methods, we do not use local isostasy to directly link the geometries of the basement and Moho. Rather, we impose smoothness on the lithostatic stress exerted by the interpretation model on a constant compensation depth, below which there are no lateral density variations. This information is directionally consistent with the basic principle of local isostatic equilibrium according to the Airy-Heiskanen and Pratt-Hayford models. Our constraint introduces the information that the lithostatic stress must be mostly smooth along the entire profile, except at some regions where it can present abrupt variations. At these locations, our method enables the estimated model to deviate from the local isostatic equilibrium. This is particularly useful for delimiting regions that conform to and deviate from the isostatic equilibrium along the profile. The second aspect by which our approach differs from those in the literature is that it allows the interpreter to control how much the estimated models can deviate from the isostatic equilibrium. As a consequence, the interpreter can obtain a set of candidate models that (1) fit the observed data and (2) present different degrees of isostatic equilibrium. Finally, it is worth noting that, in contrast to most of the earlier studies, our method attempts to use isostasy for exploring (and not necessarily reducing) the inherent ambiguity of gravity methods.

Tests with synthetic data show the good performance of our method in simultaneously retrieving the geometry of the basement and Moho of a realistic margin model presenting an extreme crustal thinning. We also applied our method to invert gravity data on a profile over the Pelotas Basin (Stica et al., 2014). This basin is located offshore of southern Brazil, and it is considered a classic example of a volcanic passive margin (Geoffroy, 2005). We inverted gravity data provided by the combined global gravity field model EIGEN-6C4 (Förste et al., 2014), one of the latest releases of the European Improved Gravity Model of the Earth by New Techniques series. Our results are consistent with the models presented by Stica et al. (2014) and Zalán (2015), who combine seismic, gravity, and magnetic data. These results show that combined with a priori information, simple isostatic models can be helpful in investigating continental margins, especially at regions presenting pronounced crustal thinning.

METHODOLOGY

Forward problem

Let \mathbf{d}^o be the observed data vector, whose i th element d_i^o , $i = 1, \dots, N$ represents the observed gravity disturbance (Heiskanen and Moritz, 1967) at the point (x_i, y_i, z_i) , on a profile located over a

rifted passive margin. The coordinates are referred to a topocentric Cartesian system, with the z -axis pointing downward, the y -axis along the profile, and the x -axis perpendicular to the profile. In local- and regional-scale studies, the gravity disturbance represents the vertical component of the gravitational attraction exerted by the gravity sources. It is more appropriate for geophysical applications, numerically similar to the classic free-air anomaly and uses the height relative to the reference ellipsoid (geometric height) instead of the geoid (orthometric height) (Li and Götze, 2001; Fairhead et al., 2003; Hackney and Featherstone, 2003; Hinze et al., 2005; Vajda et al., 2006, 2007).

The density distribution in a rifted margin can be very complex. In volcanic margins, for example, the crust may consist partially or wholly of flood-basalts and tuffs, which are commonly imaged as seaward dipping reflectors (SDRs). Underneath this intruded crust, high-velocity seismic zones are usually interpreted as bodies of underplated mafic to ultramafic magma (Geoffroy, 2005). We assume that the actual mass distribution in a rifted passive margin can be schematically represented according to Figure 1. In this model, the subsurface is formed by four layers. Layer 1 is the shallowest and represents a water layer with constant density $\rho^{(w)}$. Layer 2 is formed by Q vertically adjacent sublayers representing sediments, salt, or volcanic rocks. In our example, this layer is formed by two sublayers with constant densities $\rho^{(q)}$, $q = 1, 2$. Different models can be created by changing the number Q according to the complexity of the study area and available a priori information. In many cases, seismic data can be used to constrain the geometry of these shallow structures. Layer 3 represents the crust, and we presume that its density $\rho^{(c)}$ varies horizontally along the profile, according to a predefined function. In Figure 1, we consider that the crust density assumes two possible values. It can be equal to $\rho^{(cc)}$, which represents the continental crust, or equal to $\rho^{(oc)}$, which represents the oceanic crust. However, more complex functions representing the crust density distribution can be specified according to the interpreter's knowledge about the geology at the study area. This approach presumes that bulk values can be used to approximate the real density distribution at the deeper parts of crust. Finally, layer 4 represents a homogeneous mantle with constant density $\rho^{(m)}$. The surface separating layers 2 and 3 defines the basement relief, whereas the surface separating layers 3 and 4 defines the Moho. These surfaces are represented as the dashed white lines in Figure 1.

To define the anomalous mass distribution producing the observed gravity disturbance, we presume a reference mass distribution formed by two layers. The shallowest represents a homogeneous crust with constant density $\rho^{(r)}$. Its thickness is defined by a surface conveniently called the reference Moho (Figures 1 and 2). The deepest layer in the reference mass distribution

represents a homogeneous mantle with constant density $\rho^{(m)}$. We note that the mantle in the reference mass distribution has the same density as the mantle in our rifted margin model (Figure 1). The reference model can be thought of as the outer layers of a concentric mass distribution producing the normal gravity field. In a local scale, this concentric mass distribution is close to a stack of two Bouguer slabs.

We consider that the anomalous mass distribution producing the observed data is defined as the difference between the rifted margin model and the reference mass distribution (Figure 1). As a consequence, the anomalous mass distribution is characterized by regions with constant density contrasts. This anomalous distribution is approximated by an interpretation model formed by N columns of vertically stacked prisms (Figure 2). For convenience, we presume that there is an observed gravity disturbance over the center of each column. We consider that the prisms in the extremities of the interpretation model extend to infinity along the y -axis to prevent edge

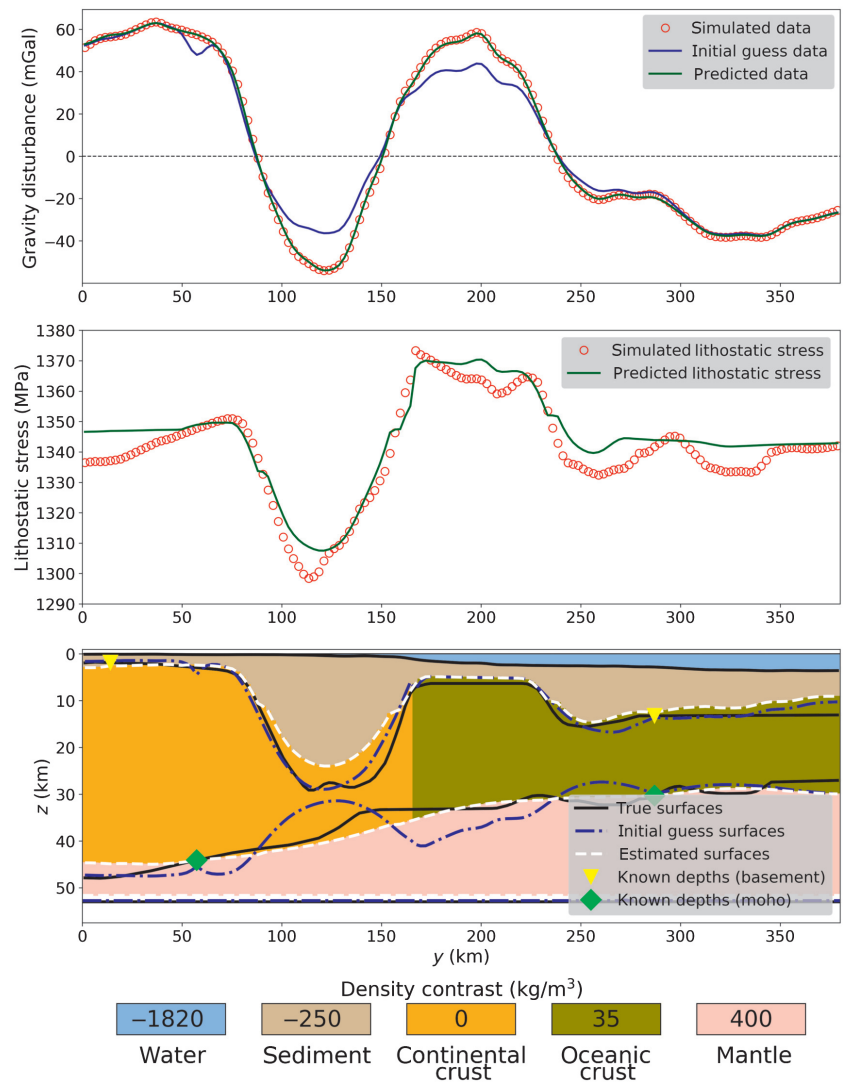


Figure 6. Application to synthetic data produced by the model based on the East Greenland margin. Estimated model $\mathbf{p}^{(3)}$ obtained at the end of step 3 (Figure 3) using $\mathbf{p}^{(2)}$ (Figure 5) as the initial approximation (the dashed blue lines) and $\sigma = 1$ (equation 23). The remaining information is the same as that shown in the caption of Figure 4.

effects in the forward calculations. The i th column is formed by vertically stacked prisms having an infinite length along the x -axis, and it locally approximates the four layers of our rifted margin model (Figure 1).

Layer 1 is defined by a single prism, and it has thickness of $t_i^{(w)}$ and a constant density contrast of $\Delta\rho^{(w)} = \rho^{(w)} - \rho^{(r)}$. Layer 2 is defined by the interpreter, according to the complexity of the study area and the available a priori information, by a set of Q vertically stacked prisms, each one with thickness of $t_i^{(q)}$ and constant density contrast of $\Delta\rho^{(q)} = \rho^{(q)} - \rho^{(r)}$, $q = 1, \dots, Q$. Layer 3 represents the deeper part of the crust; it is also formed by a single prism and has thickness of $t_i^{(c)}$ and density contrast of $\Delta\rho_i^{(c)} = \rho_i^{(c)} - \rho^{(r)}$, with $\rho_i^{(c)}$ being the crust density at the coordinate y_i , $i = 1, \dots, N$, along the profile. According to Figure 2, the crust density contrast $\Delta\rho_i^{(c)}$ may assume two possible values, depending on its position with respect to the coordinate y_{COT} of the crust-ocean transition (COT). More complex models can be set by the inter-

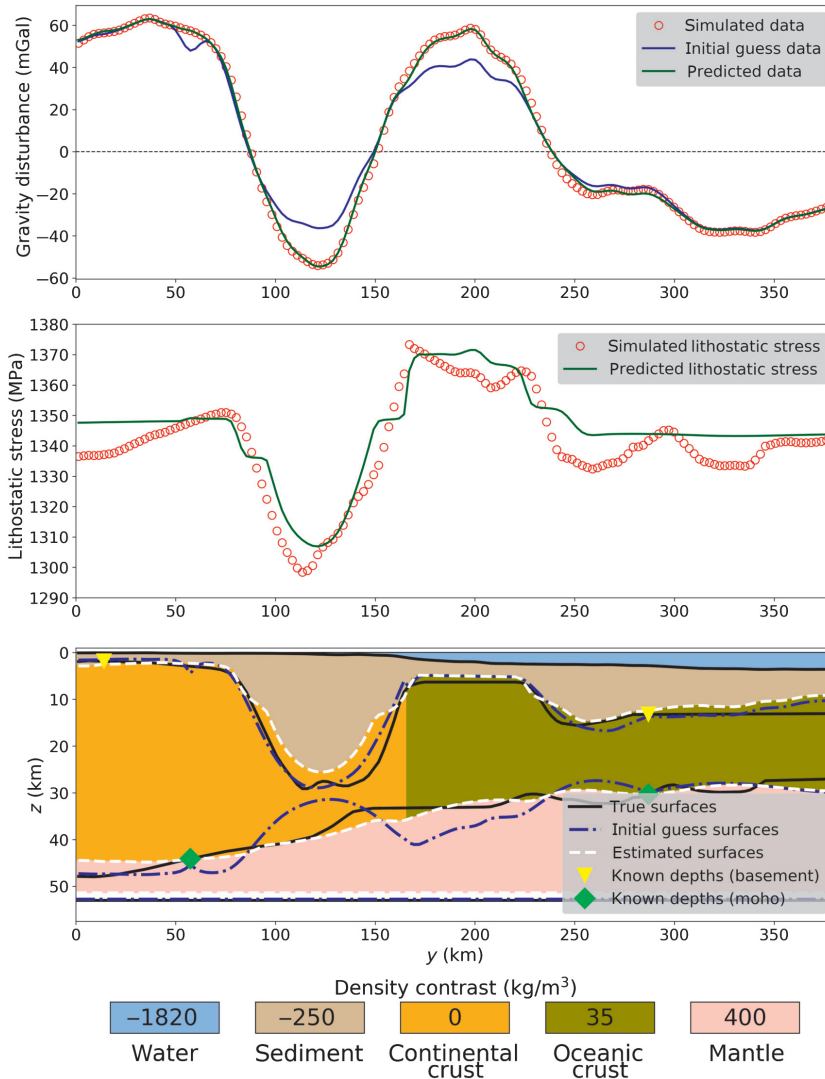


Figure 7. Application to synthetic data produced by the model based on the East Greenland margin. Estimated model $\mathbf{p}^{(3)}$ obtained at the end of step 3 (Figure 3) using $\mathbf{p}^{(2)}$ (Figure 5) as the initial approximation (the dashed blue lines) and $\sigma = 11$ (equation 23). The remaining information is the same as that shown in the caption of Figure 4.

preter according to the available a priori information at the study area. The top and bottom of this layer define, respectively, the basement and Moho. Finally, layer 4 representing the mantle is divided into two sublayers, each one formed by a single prism having the same constant density contrast $\Delta\rho^{(m)} = \rho^{(m)} - \rho^{(r)}$. The shallowest sublayer has thickness $t_i^{(m)}$. Its top and bottom define, respectively, the depths of Moho and the compensation depth S_0 . The deepest sublayer has thickness ΔS , top at S_0 and bottom at $S_0 + \Delta S$, which defines the reference Moho.

Given the density contrasts, the COT position y_{COT} , the compensation depth S_0 , the thickness $t_i^{(w)}$ of the prisms defining layer 1 and also the thickness $t_i^{(q)}$, $i = 1, \dots, N$, of the prisms forming the upper $Q - 1$ sublayers of layer 2, it is possible to describe the interpretation model in terms of an $M \times 1$ parameter vector \mathbf{p} , $M = 2N + 1$, defined as follows:

$$\mathbf{p} = \begin{bmatrix} \mathbf{t}^{(Q)} \\ \mathbf{t}^{(m)} \\ \Delta S \end{bmatrix}, \quad (1)$$

where $\mathbf{t}^{(Q)}$ and $\mathbf{t}^{(m)}$ are the $N \times 1$ vectors whose i th elements $t_i^{(Q)}$ and $t_i^{(m)}$ (Figure 2) represent the thickness of the prisms forming, respectively, the base of layer 2 and the top of layer 4. Note that $t_i^{(Q)}$ and $t_i^{(m)}$, $i = 1, \dots, N$, approximate, respectively, the geometries of the basement and Moho and ΔS defines the depth of the reference Moho (Figure 2). In this case, the gravity disturbance produced by the interpretation model (the predicted gravity disturbance) at the position (x_i, y_i, z_i) can be written as the sum of the vertical component of the gravitational attraction exerted by the L prisms forming the interpretation model as follows:

$$d_i(\mathbf{p}) = k_g G \sum_{j=1}^L f_{ij}(\mathbf{p}), \quad (2)$$

where k_g transforms m/s^2 to mGal , G is the gravitational constant and $f_{ij}(\mathbf{p})$ represents an integral over the volume of the j th prism. Here, these volume integrals are computed with the expressions proposed by Nagy et al. (2000), using the open-source Python package Fatiando a Terra (Uieda et al., 2013).

Inverse problem formulation

Let $\mathbf{d}(\mathbf{p})$ be the predicted data vector, whose i th element $d_i(\mathbf{p})$ is the vertical component of the gravitational attraction (equation 2) exerted by the interpretation model at the position (x_i, y_i, z_i) on the profile. We estimate a particular parameter vector producing a predicted data $\mathbf{d}(\mathbf{p})$ as close as possible to the observed data \mathbf{d}^o by minimizing the goal function:

$$\Gamma(\mathbf{p}) = \Phi(\mathbf{p}) + \sum_{\ell=0}^4 \mu_\ell \Psi_\ell(\mathbf{p}), \quad (3)$$

subject to the inequality constraint

$$p_j^{\min} < p_j < p_j^{\max}, \quad j = 1, \dots, M \quad (4)$$

where p_j^{\min} and p_j^{\max} define, respectively, the lower and upper bounds for the j th element of \mathbf{p} . In equation 3, μ_ℓ is the weight assigned to the ℓ th regularizing function $\Psi_\ell(\mathbf{p})$, $\ell = 0, \dots, 4$, and $\Phi(\mathbf{p})$ is the misfit function given by

$$\Phi(\mathbf{p}) = \frac{1}{N} \|\mathbf{d}^o - \mathbf{d}(\mathbf{p})\|_2^2, \quad (5)$$

where $\|\cdot\|_2^2$ represents the squared Euclidean norm. Note that our method estimates the parameter vector \mathbf{p} (equation 1), which contains the geometries of the basement and Moho, as well as the thickness ΔS defining the depth of the reference Moho (Figure 2). The bottom of layer 1 is defined by the available bathymetry. The geometry of the upper sublayers forming layer 2 and the constant compensation depth S_0 (Figure 2) are defined using the available a priori information. These predefined quantities remain fixed during the inversion. Details about the regularizing functions $\Psi_\ell(\mathbf{p})$, $\ell = 0, \dots, 4$ and the numerical procedure to solve this nonlinear inverse problem are given in the following sections.

Isostatic constraint

Consider that no vertical forces are acting on the lateral surfaces of each column forming the model (Figure 2). In this case, the lithostatic stress (pressure) τ_i (in MPa) exerted by the i th column at surface S_0 can be computed according to Archimedes' principle as follows (Turcotte and Schubert, 2002, p. 129):

$$t_i^{(w)} \rho_i^{(w)} + t_i^{(1)} \rho_i^{(1)} + \dots + t_i^{(Q)} \rho_i^{(Q)} + t_i^{(c)} \rho_i^{(c)} + t_i^{(m)} \rho_i^{(m)} = \tau_i g_m^{-1}, \quad (6)$$

where g_m is the mean gravity value of the study area. We consider this mean value equal to 9.81 m/s^2 along the profile. By rearranging terms in equation 6 and using the relation

$$S_0 = t_i^{(w)} + t_i^{(1)} + \dots + t_i^{(Q)} + t_i^{(c)} + t_i^{(m)}, \quad (7)$$

it is possible to show that

$$\Delta \tilde{\rho}_i^{(Q)} t_i^{(Q)} + \Delta \tilde{\rho}_i^{(m)} t_i^{(m)} + \Delta \tilde{\rho}_i^{(w)} t_i^{(w)} + \Delta \tilde{\rho}_i^{(1)} t_i^{(1)} + \dots + \Delta \tilde{\rho}_i^{(Q-1)} t_i^{(Q-1)} + \rho_i^{(c)} S_0 = \tau_i g_m^{-1}, \quad (8)$$

where $\Delta \tilde{\rho}_i^{(\alpha)} = \rho_i^{(\alpha)} - \rho_i^{(c)}$, $\alpha = w, 1, \dots, Q-1, Q, m$. To describe the lithostatic stress exerted by all columns forming the interpretation model on the surface S_0 , equation 8 can be written as follows:

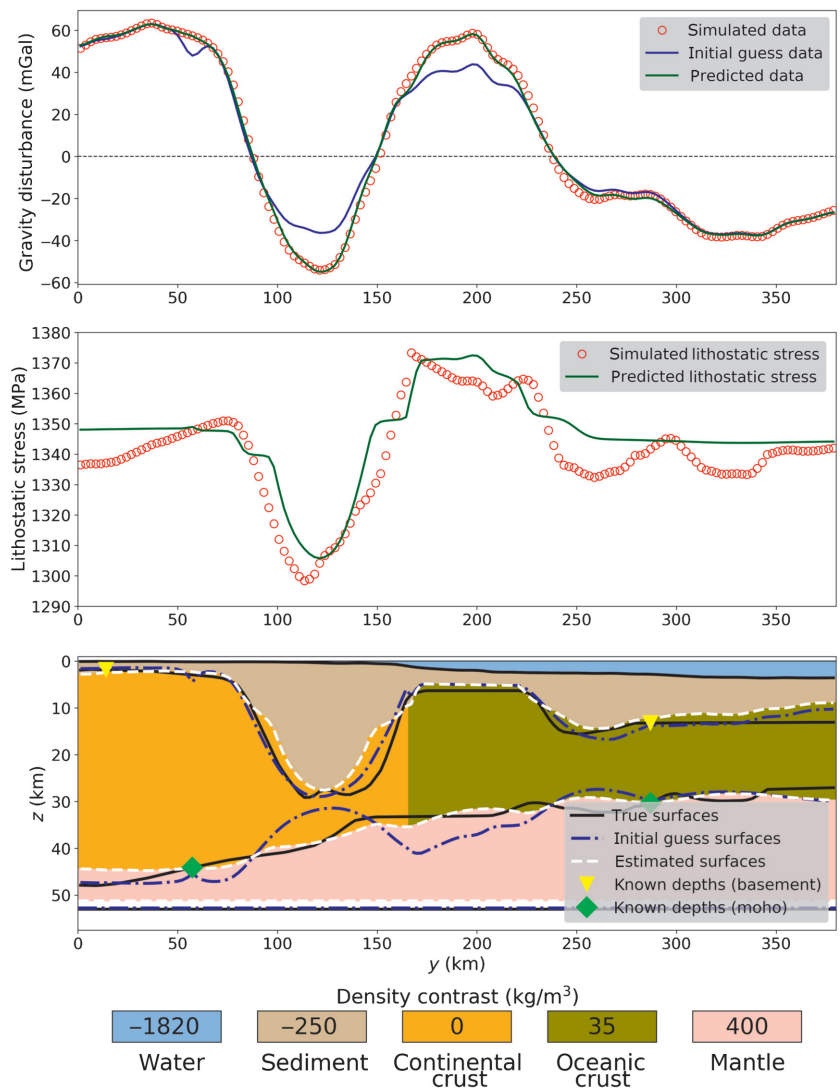


Figure 8. Application to synthetic data produced by the model based on the East Greenland margin. Estimated model $\mathbf{p}^{(3)}$ obtained at the end of step 3 (Figure 3) using $\mathbf{p}^{(2)}$ (Figure 5) as the initial approximation (the dashed blue lines) and $\sigma = 18$ (equation 23). The remaining information is the same as that shown in the caption of Figure 4.

Table 2. Properties of the simple synthetic margin model.

Geologic meaning	$\rho^{(\alpha)}$ (kg/m^3)	$\Delta \rho^{(\alpha)}$ (kg/m^3)	α
Water	1030	-1790	w
Sediments	2600	-190	1
Continental crust	2790	0	cc
Oceanic crust	2880	90	oc
Mantle	3250	460	m

The model extends from $y = 0 \text{ km}$ to $y = 250 \text{ km}$, the COT is located at $y_{\text{COT}} = 170 \text{ km}$, and the reference Moho is located at 46 km (Figures 1 and 2). The density contrasts $\Delta \rho^{(\alpha)} = \rho^{(\alpha)} - \rho^{(r)}$ were defined using the reference value $\rho^{(r)} = 2790 \text{ kg/m}^3$, which coincides with the density $\rho^{(cc)}$ attributed to the continental crust.

$$\mathbf{M}^{(Q)}\mathbf{t}^{(Q)} + \mathbf{M}^{(m)}\mathbf{t}^{(m)} + \mathbf{M}^{(w)}\mathbf{t}^{(w)} + \mathbf{M}^{(1)}\mathbf{t}^{(1)} + \dots + \mathbf{M}^{(Q-1)}\mathbf{t}^{(Q-1)} + \mathbf{\rho}^{(c)}S_0 = g_m^{-1}\boldsymbol{\tau}, \quad (9)$$

where $\boldsymbol{\tau}$ is an $N \times 1$ vector whose i th element is the τ_i (equation 6) associated with the i th column; $\mathbf{t}^{(\alpha)}$, $\alpha = w, 1, \dots, Q-1, Q, m$, is an $N \times 1$ vector with i th element defined by the thickness $t_i^{(\alpha)}$ of a prism in the i th column; $\mathbf{M}^{(\alpha)}$ is an $N \times N$ diagonal matrix whose elements are defined by the density contrasts $\Delta\tilde{\rho}_i^{(\alpha)}$, $i = 1, \dots, N$, of the prisms in a layer; and $\mathbf{\rho}^{(c)}$ is an $N \times 1$ vector containing the densities of the prisms representing the crust. The term $g_m^{-1}\boldsymbol{\tau}$ describing the lithostatic stress exerted by all prisms on S_0 is conveniently called the lithostatic stress curve.

Let us now use an approach similar to that presented by Ferderer et al. (2017) to combine the Airy-Heiskanen and Pratt-Hayford mod-

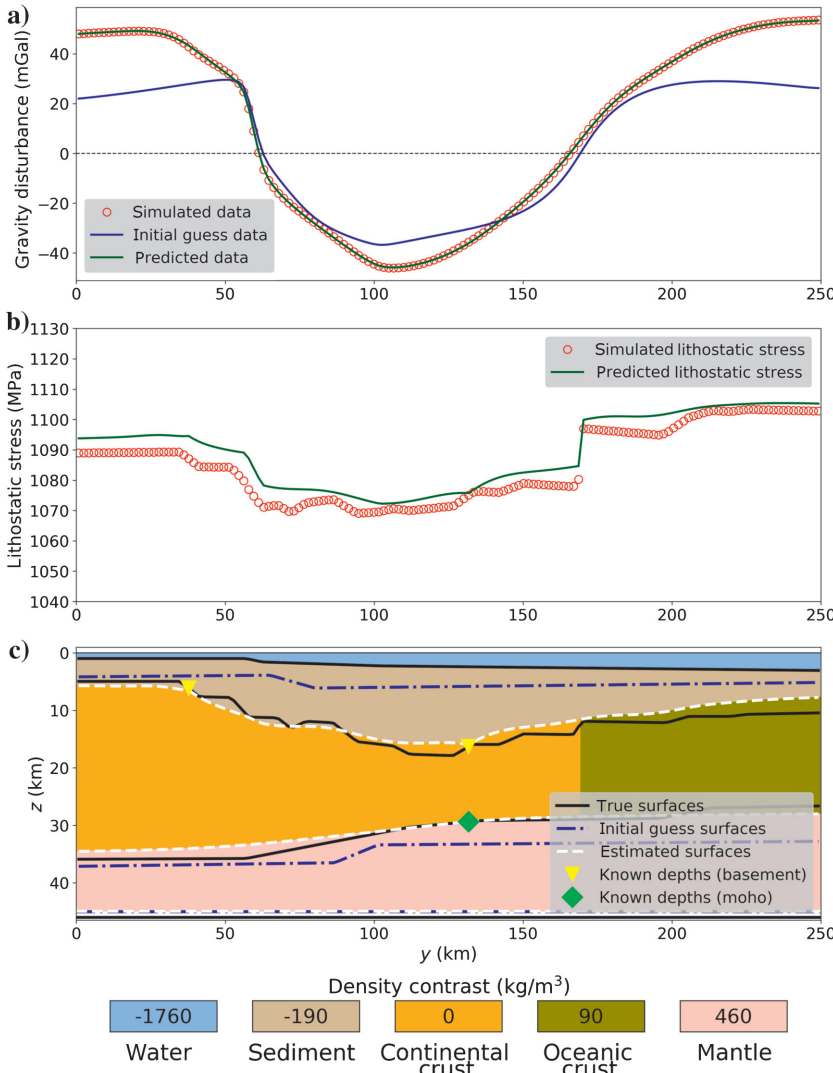


Figure 9. Application to synthetic data produced by a simple model. Estimated model $\mathbf{p}^{(1)}$ obtained at the end of step 1 (Figure 3) using $\tilde{\mu}_1 = 10^1$, $\tilde{\mu}_2 = 10^2$, $\tilde{\mu}_3 = 10^1$, and $\tilde{\mu}_4 = 10^2$. (c) True and estimated surfaces, initial basement and Moho (initial guess) and a priori information at points on the basement and Moho (known depths). (b) True and predicted lithostatic stress curves (equation 9). (a) Gravity disturbance produced by the true model (simulated data), by the estimated model (predicted data), and by the initial guess (initial guess data). The density contrasts are those shown in Table 2 and $S_0 = 40$ km.

els (Heiskanen and Moritz, 1967) to impose local isostatic equilibrium. We impose this condition by varying density and geometry of the crust along the rifted margin. In this case, the lithostatic stress exerted by the interpretation model must be constant at the compensation depth S_0 (Figure 2). Different from previous approaches in the literature, we impose isostatic equilibrium by forcing the lithostatic stress to be smooth at S_0 . We apply the first-order Tikhonov regularization (Aster et al., 2005) to the lithostatic stress curve $g_m^{-1}\boldsymbol{\tau}$ (equation 9), obtaining the following expression:

$$\mathbf{R}(\mathbf{Cp} + \mathbf{Dt}) = \mathbf{0}, \quad (10)$$

where $\mathbf{0}$ is a vector with null elements and the remaining terms are given by

$$\mathbf{C} = [\mathbf{M}^{(Q)} \quad \mathbf{M}^{(m)} \quad \mathbf{0}]_{N \times M}, \quad (11)$$

$$\mathbf{D} = [\mathbf{M}^{(w)} \quad \mathbf{M}^{(1)} \quad \dots \quad \mathbf{M}^{(Q-1)} \quad \mathbf{\rho}^{(c)}]_{N \times (QN+1)}, \quad (12)$$

$$\mathbf{t} = \begin{bmatrix} \mathbf{t}^{(w)} \\ \mathbf{t}^{(1)} \\ \vdots \\ \mathbf{t}^{(Q-1)} \\ S_0 \end{bmatrix}_{(QN+1) \times 1}, \quad (13)$$

and \mathbf{R} is an $(N-1) \times N$ matrix, whose element i,j is defined as follows:

$$[\mathbf{R}]_{ij} = \begin{cases} 1, & j = i \\ -1, & j = i + 1 \\ 0, & \text{otherwise} \end{cases}. \quad (14)$$

Finally, from equation 10, it is possible to define the regularizing function $\Psi_0(\mathbf{p})$ (equation 3)

$$\Psi_0(\mathbf{p}) = \|\mathbf{WR}(\mathbf{Cp} + \mathbf{Dt})\|_2^2, \quad (15)$$

where \mathbf{W} is an $(N-1) \times (N-1)$ diagonal matrix having constant elements $0 < w_{ii} \leq 1$, $i = 1, \dots, N-1$. Function $\Psi_0(\mathbf{p})$ defines the isostatic constraint.

We note that by minimizing the function $\Psi_0(\mathbf{p})$ (equation 15), the method imposes smoothness on the lithostatic stress exerted by the interpretation model on the compensation depth S_0 . Matrix \mathbf{W} controls the relative amount of isostatic equilibrium imposed along the profile. In the particular case in which all diagonal elements w_{ii} have the same constant value, the same amount of isostatic equilibrium is imposed along the whole profile. On the other hand, different amounts of isostatic equilibrium can be imposed along the profile by varying the values

of these elements. Elements $w_{ii} \approx 1$ impose a smooth lithostatic stress curve at the transition between columns i and $i + 1$ of the interpretation model. Elements $w_{ii} \approx 0$ allow abrupt variations in the lithostatic stress curve between columns i and $i + 1$ of the interpretation model. Using all elements $w_{ii} = 1$, we impose full isostatic equilibrium along the entire profile. Alternatively, we may enable the interpretation model to deviate from the isostatic equilibrium by conveniently decreasing the numerical values assigned to the elements w_{ii} at specific regions along the profile. The strategy used to define the elements w_{ii} is presented in the specific section describing the computational procedures for solving the inverse problem.

Smoothness constraints

These constraints impose smoothness on the adjacent thickness of the prisms defining the geometries of the basement (base of layer 2) and Moho (top of layer 4). This information is introduced by applying the first-order Tikhonov regularization (Aster et al., 2005) to the vectors $\mathbf{t}^{(Q)}$ and $\mathbf{t}^{(m)}$ (equation 1). Mathematically, these constraints are represented by the regularizing functions $\Psi_1(\mathbf{p})$ and $\Psi_2(\mathbf{p})$ (equation 3), which are given by

$$\Psi_1(\mathbf{p}) = \|\mathbf{Sp}\|_2^2 \quad (16)$$

and

$$\Psi_2(\mathbf{p}) = \|\mathbf{Tp}\|_2^2, \quad (17)$$

where \mathbf{S} and \mathbf{T} are the matrices given by

$$\mathbf{S} = [\mathbf{R} \quad \mathbf{0} \quad \mathbf{0}]_{(N-1) \times M} \quad (18)$$

and

$$\mathbf{T} = [\mathbf{0} \quad \mathbf{R} \quad \mathbf{0}]_{(N-1) \times M}. \quad (19)$$

In these equations, \mathbf{R} is defined in equation 14 and $\mathbf{0}$ are matrices with all elements being equal to zero.

Equality constraints

To incorporate a priori information at isolated points on the basement and Moho surfaces, we use an approach similar to those proposed by Barbosa et al. (1997, 1999a).

Equality constraint on vector $\mathbf{t}^{(Q)}$

Let \mathbf{a} be a vector whose k th element a_k , $k = 1, \dots, A$, is the difference between a known basement depth and the sum of the thickness of the upper parts of the interpretation model (the water layer and the upper sublayers of layer 2), all at the same horizontal coordinate y_k^A of the profile. These differences, which must be positive, are used to define the regularizing function $\Psi_2(\mathbf{p})$ (equation 3):

$$\Psi_2(\mathbf{p}) = \|\mathbf{Ap} - \mathbf{a}\|_2^2, \quad (20)$$

where \mathbf{A} is an $A \times M$ matrix whose k th line has one element equal to one and all the remaining elements equal zero. The location of the single nonnull element in the k th line of \mathbf{A} depends on the coordinate y_k^A of the known thickness a_k . Let us consider, for example, an interpretation model formed by $N = 10$ columns. Consider also that the thicknesses of the deepest sublayer of layer 2 at the coordinates $y_1^A = y_4$ and $y_2^A = y_9$ are equal to 25 and 35.7 km, respectively. In this case, $A = 2$, \mathbf{a} is a 2×1 vector with elements $a_1 = 25$ and $a_2 = 35.7$, and \mathbf{A} is a $2 \times M$ matrix ($M = 2N + 1 = 21$). Element 4 of the first line and the element 9 of the second line of \mathbf{A} are equal to 1, and all its remaining elements are equal to zero.

Equality constraint on vector $\mathbf{t}^{(m)}$

Let \mathbf{b} be a vector whose k th element b_k , $k = 1, \dots, B$, is the difference between the compensation depth S_0 and the known Moho

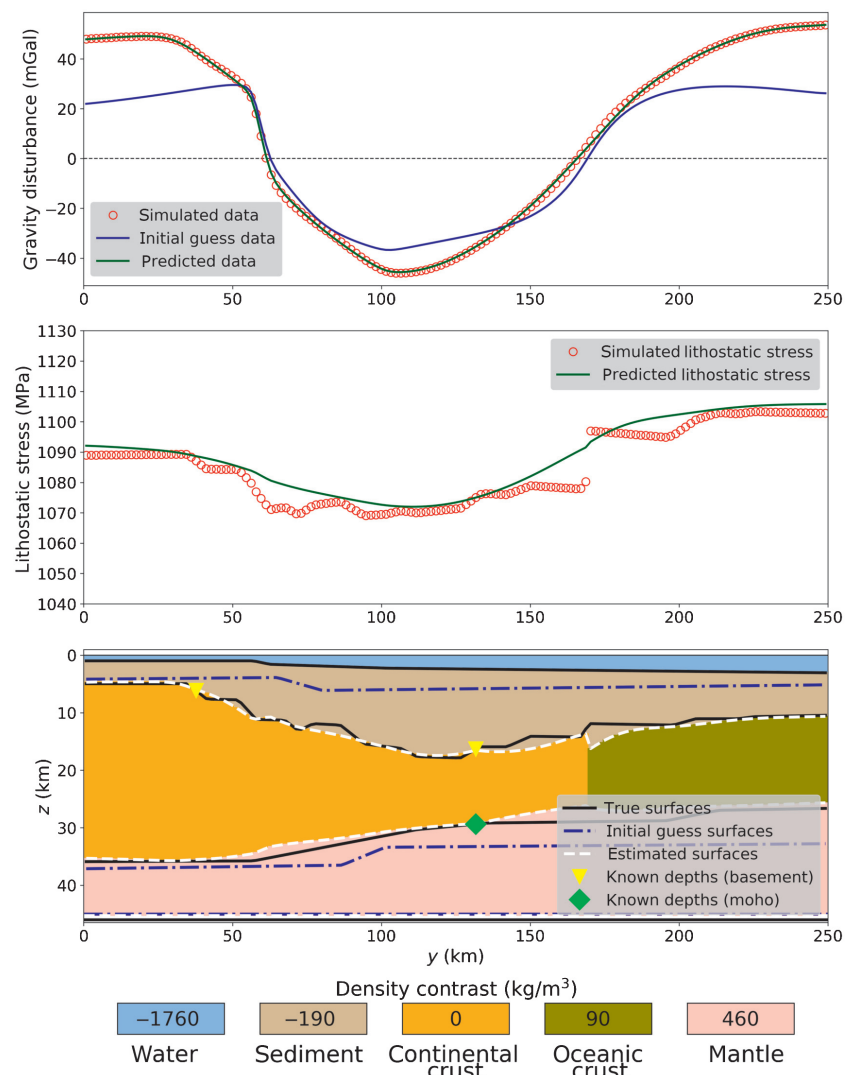


Figure 10. Application to synthetic data produced by a simple model. Estimated model $\mathbf{p}^{(2)}$ obtained at the end of step 2 (Figure 3) using $\tilde{\mu}_0 = 10^2$. The remaining information is the same as that shown in the caption of Figure 9.

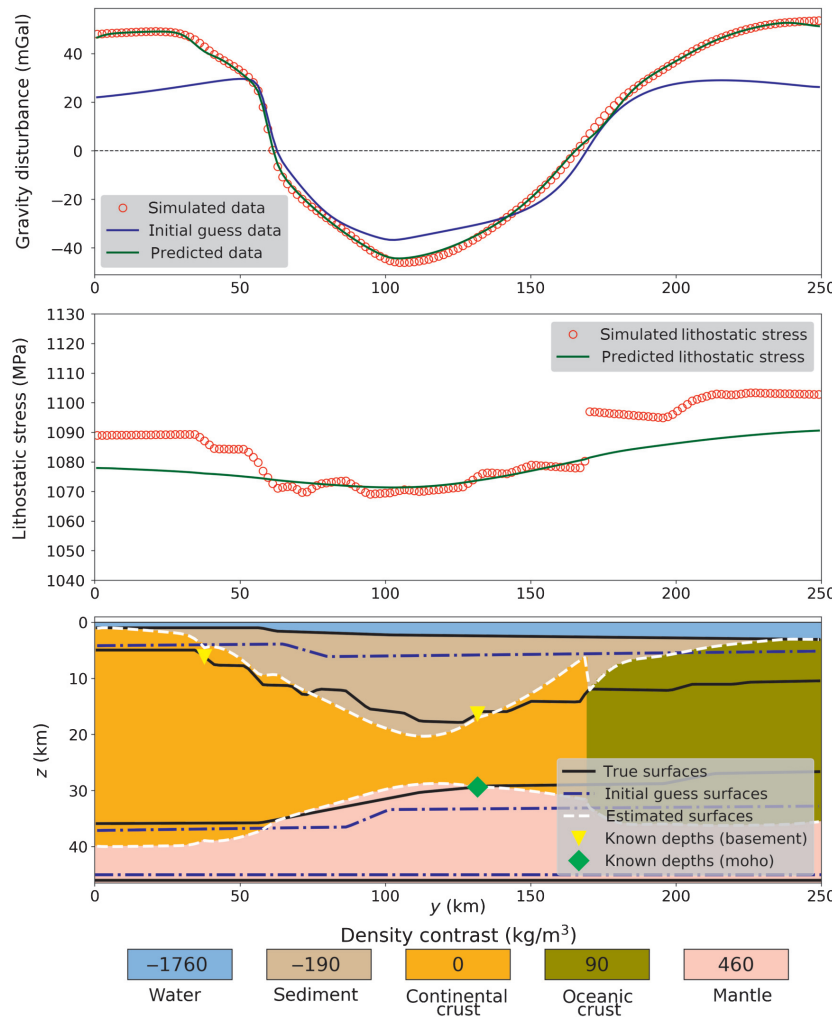


Figure 11. Application to synthetic data produced by a simple model. Estimated model $\mathbf{p}^{(2)}$ obtained at the end of step 2 (Figure 3) using $\tilde{\mu}_0 = 10^5$. The remaining information is the same as that shown in the caption of Figure 9.

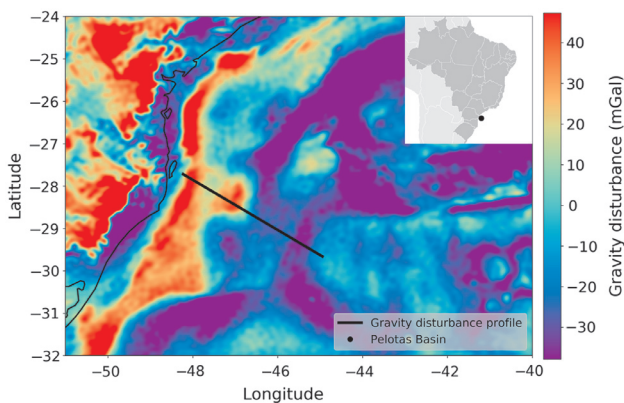


Figure 12. Application to real data on Pelotas Basin, Brazil. Gravity disturbance provided by the global gravity field model EIGEN-6C4 (Förste et al., 2014) at the study area. The black straight line indicates the gravity profile over the Pelotas Basin. The end points of the profile have coordinates (geodetic latitude and longitude) $(-27.72^\circ, -48.23^\circ)$ and $(-29.66^\circ, -44.94^\circ)$. The coordinates of the figure are referred to the ellipsoid WGS84, which is a geodetic datum.

depth at the horizontal coordinate y_k^B of the profile. These differences, which must be positive, define the known thickness values of the upper part of layer 4. These values are used to define the regularizing function $\Psi_3(\mathbf{p})$ (equation 3):

$$\Psi_3(\mathbf{p}) = \|\mathbf{B}\mathbf{p} - \mathbf{b}\|_2^2, \quad (21)$$

where \mathbf{B} is a $B \times M$ matrix whose k th line has one element equal to one and all the remaining elements equal to zero. This matrix is defined in the same way as matrix \mathbf{A} (equation 20).

Computational procedures for solving the inverse problem

The parameter vector \mathbf{p} (equation 1) minimizing the goal function $\Gamma(\mathbf{p})$ (equation 3), subjected to the inequality constraint (equation 4), is estimated in three steps (steps 1, 2, and 3 are described in the following subsections). At each step, the goal function is minimized using the Levenberg-Marquardt method (Silva et al., 2001; Aster et al., 2005), and the inequality constraint (equation 4) is incorporated using the same strategy used by Barbosa et al. (1999b). All derivatives of the misfit function $\Phi(\mathbf{p})$ (equation 5) with respect to the parameters are computed using a finite-difference approximation.

Considerations about the weights μ_0 , μ_1 , μ_2 , μ_3 , and μ_4

An important aspect of our method is related to the values attributed to the weights μ_ℓ (equation 3). Their values can be dependent on the particular characteristics of the interpretation model, and there is no analytical rule to define them. To overcome this problem, we normalize the μ_ℓ values as follows:

$$\mu_\ell = \tilde{\mu}_\ell \frac{E_\Phi}{E_\ell}, \quad \ell = 0, \dots, 4, \quad (22)$$

Table 3. Properties used in the Pelotas volcanic margin.

Geologic meaning	$\rho^{(a)}$ (kg/m³)	$\Delta\rho^{(a)}$ (kg/m³)	α
Water	1030	-1840	w
Sediments	2350	-520	1
SDR	2855	-15	2
Continental crust	2870	0	cc
Oceanic crust	2885	15	oc
Mantle	3240	370	m

The interpretation model extends from $y = 0$ km to $y = 383$ km, the COT is located at $y_{\text{COT}} = 350$ km, and the reference Moho is located at 43,200 km (Figures 1 and 2). The density contrasts $\Delta\rho^{(a)} = \rho^{(a)} - \rho^{(r)}$ were defined using the reference value $\rho^{(r)} = 2870$ kg/m³, which coincides with the density $\rho^{(cc)}$ attributed to the continental crust.

where $\tilde{\mu}_\ell$ is a positive scalar and E_Φ/E_ℓ is a normalizing constant. In this equation, E_ℓ represents the median of the elements forming the main diagonal of the Hessian matrix of the ℓ th constraining function $\Psi_\ell(\mathbf{p})$ (equations 15, 16, 17, 20, and 21). The constant E_Φ is defined in a similar way using the Hessian matrix of the misfit function $\Phi(\mathbf{p})$ (equation 5) computed with the initial approximation $\mathbf{p}^{(0)}$ for the parameter vector \mathbf{p} (equation 1) at step 1 (described in the following subsection). According to this empirical strategy, the weights μ_ℓ are defined using the positive scalars $\tilde{\mu}_\ell$ (equation 22), which are less dependent on the particular characteristics of the interpretation model.

Step 1

This step is represented in blue at the flow diagram shown in Figure 3. It consists of solving the inverse problem without imposing the isostatic constraint, using $\tilde{\mu}_0 = 0$ (equation 22). At this step, the interpreter must set

- Parameters defining the interpretation model (Figure 2): density contrasts $\Delta\rho^{(\alpha)}$, $\alpha = w, 1, \dots, Q, cc, oc, m$, COT position y_{COT} , thickness $t_i^{(w)}$ of the prisms defining layer 1, thickness $t_i^{(q)}$, $i = 1 \dots, N$, of the prisms forming the upper $Q - 1$ sublayers of layer 2, and the isostatic compensation depth S_0 . Figure 2 illustrates the case in which the second layer is formed by $Q = 2$ parts. This number, however, can be changed according to the study area.
- Parameters for the inversion: weights $\tilde{\mu}_\ell$, $\ell = 1, \dots, 4$ (equation 22), associated to the smoothness and equality constraints (equations 16, 17, 20, and 21), lower and upper bounds p_j^{\min} and p_j^{\max} (equation 4), $j = 1, \dots, M$, for the parameters to be estimated, vectors \mathbf{a} (equation 20) and \mathbf{b} (equation 21) containing known thickness values and an initial approximation $\mathbf{p}^{(0)}$ for the parameter vector \mathbf{p} (equation 1). The initial approximation $\mathbf{p}^{(0)}$ must satisfy the inequality constraints (equation 4).

The initial approximation $\mathbf{p}^{(0)}$ is used to compute the Hessian matrix of the misfit function $\Phi(\mathbf{p})$ (equation 5), which is subsequently used to compute the constant E_Φ (equation 22). The estimated parameter vector obtained at the end of step 1 is conveniently called $\mathbf{p}^{(1)}$. The main goal in this step is finding suitable values for the parameters defining the interpretation model and those used for inversion. Several trials may be necessary to find suitable values for these parameters.

Step 2

Step 2 is represented in red at the flow diagram (Figure 3) and consists of obtaining an estimated

parameter vector $\mathbf{p}^{(2)}$ by imposing full isostatic equilibrium on the interpretation model along the entire profile. In this step, the interpreter must use the same initial approximation $\mathbf{p}^{(0)}$ of step 1. In addition, the interpreter must set matrix \mathbf{W} equal to the identity and find a suitable value for weight $\tilde{\mu}_0$ (equation 22) controlling the isostatic constraint (equation 15). We presume that, by imposing full isostatic equilibrium along the entire profile, the estimated parameter vector $\mathbf{p}^{(2)}$ will produce a mostly good data fit, except at some isolated regions. We assume that, at these regions, the passive margin deviates from the local isostatic equilibrium.

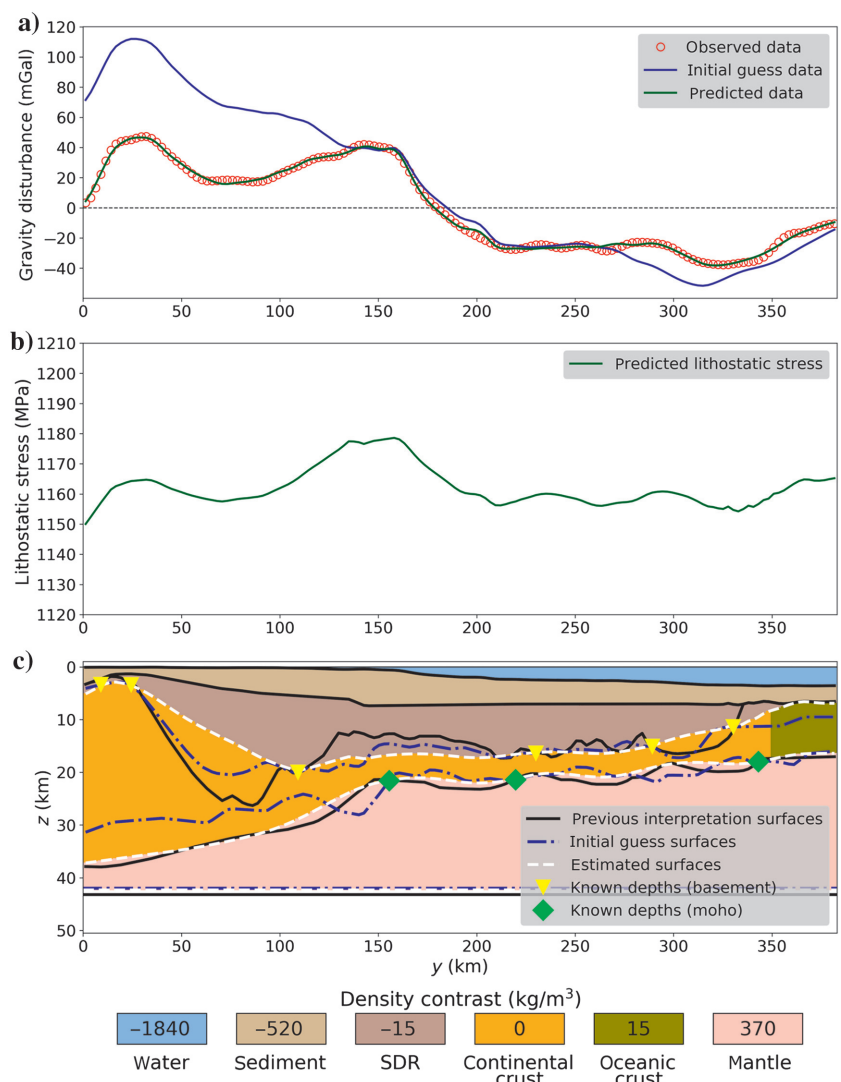


Figure 13. Application to real data from the Pelotas Basin, Brazil. Estimated model $\mathbf{p}^{(1)}$ obtained at the end of step 1 (Figure 3) using $\tilde{\mu}_1 = 10^1$, $\tilde{\mu}_2 = 10^2$, $\tilde{\mu}_3 = 10^1$, and $\tilde{\mu}_4 = 10^2$. (c) Estimated surfaces, initial basement and Moho (initial guess), and a priori information at the basement and Moho (known depths). The continuous black lines represent a previous interpretation presented by Zalán (2015). (b) True and predicted lithostatic stress curves (equation 9). (a) Observed gravity disturbance, data produced by the estimated model (predicted data), and data produced by the initial approximation (initial guess data). We used $S_0 = 41$ km, density contrasts equal to those shown in Table 3, and an initial approximation for ΔS equal to 1 km.

Step 3

Step 3 is represented in green at the flow diagram (Figure 3). It consists of using $\mathbf{p}^{(2)}$ as the initial approximation to obtain an estimated parameter vector $\mathbf{p}^{(3)}$ by imposing different amounts of isostatic equilibrium on the interpretation model along the profile. At this step, the interpreter must compute the diagonal elements w_{ii} of the matrix \mathbf{W} (equation 15) to enable the interpretation model to deviate from isostatic equilibrium in the regions presenting large residuals. The elements of \mathbf{W} are computed as follows:

$$w_{ii} = \exp\left[-\frac{(r_i^{(2)} + r_{i+1}^{(2)})^2}{4\sigma}\right], \quad (23)$$

where σ is a positive constant, $\mathbf{p}^{(2)}$ is the estimated parameter vector obtained in the previous step, and the variables $r_i^{(2)} = d_i^o - d_i(\mathbf{p}^{(2)})$ and $r_{i+1}^{(2)} = d_{i+1}^o - d_{i+1}(\mathbf{p}^{(2)})$ represent, respectively, the residuals

between the observed and predicted data (equation 2) at the positions (x_i, y_i, z_i) and $(x_{i+1}, y_{i+1}, z_{i+1})$. Note that equation 23 defines elements w_{ii} in the interval $]0, 1]$. In addition, this equation results in $w_{ii} \approx 1$ at regions where the residuals are close to zero and $w_{ii} \approx 0$ at regions presenting large residuals. The positive constant σ controls the deviation from isostatic equilibrium. Small σ values allow large deviations from isostatic equilibrium, resulting in estimated models close to that obtained at step 1. Large σ values allow small deviations from isostatic equilibrium, resulting in estimated models close to that obtained at step 2. This strategy to define the elements of matrix \mathbf{W} (equation 15) presumes that the isostatic constraint may produce large residuals at some regions along the profile. To counteract this problem, our method enables the interpretation model to deviate from isostatic equilibrium at these regions. This idea is in agreement with the observation that isostatic equilibrium at a passive rifted margin cannot be totally explained by local models.

Practical considerations

Our algorithm depends on several parameters that significantly impact the estimated models and cannot be automatically set without the interpreter's judgment. They are the parameters $\tilde{\mu}_1, \tilde{\mu}_2, \tilde{\mu}_3$, and $\tilde{\mu}_4$ (step 1), $\tilde{\mu}_0$ (step 2), and σ (step 3). Based on our practical experience, we suggest some empirical procedures for setting these parameters at each step. They are schematically represented in the flow diagram (Figure 3).

At step 1, set $\tilde{\mu}_1 = \tilde{\mu}_2 = 0$ and try different positive values for $\tilde{\mu}_3$ and $\tilde{\mu}_4$. These two parameters control the equality constraints (equations 20 and 21) imposing a priori information at isolated points on the basement and Moho surfaces. Good starting values are, respectively, 10^1 and 10^2 . Normally, $\tilde{\mu}_4$ is one order of magnitude greater than $\tilde{\mu}_3$. The parameters $\tilde{\mu}_3$ and $\tilde{\mu}_4$ must be the smallest positive numbers resulting in an estimated model \mathbf{p}' with basement and Moho surfaces close to the values provided by the a priori information at some isolated points. Note that \mathbf{p}' is an intermediate model obtained using only the equality constraints. Consequently, there must be some pinnacles in the estimated models, around the points associated with the a priori information. This effect has already been observed by Barbosa et al. (1997). The acceptability criterion described earlier to define the values of $\tilde{\mu}_3$ and $\tilde{\mu}_4$ is represented by the decision point $D(\tilde{\mu}_3, \tilde{\mu}_4)$ in the flow diagram (Figure 3).

Using the chosen values for $\tilde{\mu}_3$ and $\tilde{\mu}_4$, try different positive values for $\tilde{\mu}_1$ and $\tilde{\mu}_2$. These parameters control the smoothness of the basement and Moho surfaces (equations 16 and 17). Usually, $\tilde{\mu}_2$ is one order of magnitude greater than $\tilde{\mu}_1$. Good starting values are 10^1 and 10^2 . These parameters must be the smallest positive numbers producing an estimated model satisfying the following conditions: (1) The data fit must be good along the entire profile and (2) the pinnacles

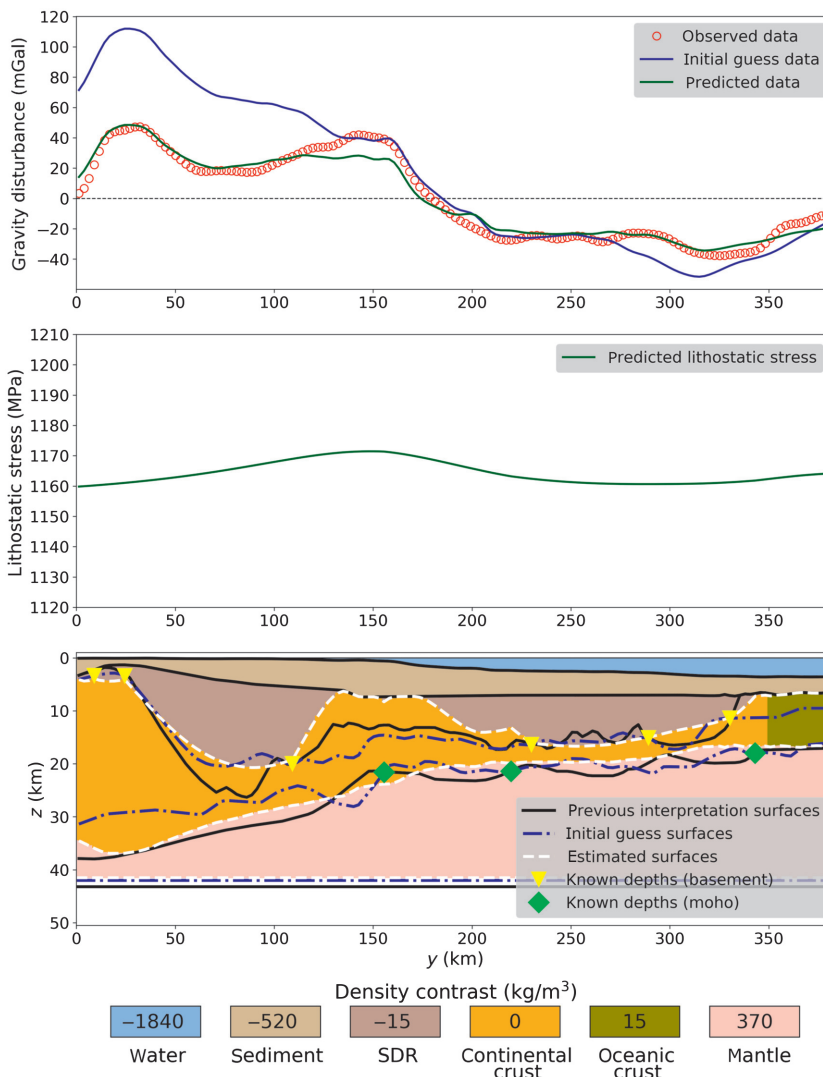


Figure 14. Application to real data from the Pelotas Basin, Brazil. Estimated model $\mathbf{p}^{(2)}$ obtained at the end of step 2 (Figure 3) using $\tilde{\mu}_0 = 10^2$. The remaining information is the same as that shown in the caption of Figure 13.

must be completely removed or attenuated as much as possible. This acceptability criterion to define the values of $\tilde{\mu}_1$ and $\tilde{\mu}_2$ is represented by the decision point $D(\tilde{\mu}_1, \tilde{\mu}_2)$ at the flow diagram (Figure 3). In general, the estimated lithostatic stress curve at step 1 is close to the true one and can be used to perform a preliminary analysis of the isostatic equilibrium along the profile. It can be used to identify regions closer to the local isostatic equilibrium, where the curve is relatively smooth and shows small variations, and regions that deviate from the equilibrium and show large variations in the lithostatic stress curve.

At step 2, try different positive values for $\tilde{\mu}_0$ (equation 22). This parameter controls the smoothness of the lithostatic stress exerted by the interpretation model at the compensation depth S_0 . In general, $\tilde{\mu}_0$ is one or two orders of magnitude greater than $\tilde{\mu}_1$. Good starting values are 10^2 or 10^3 . This parameter must be the largest positive number resulting in an estimated model satisfying two conditions: (1) The lithostatic stress curve must be smoother than that obtained at step 1 along the entire profile, and (2) there must be a good data fit along the entire profile, except at some isolated regions that may show relatively large residuals. This acceptability criterion for the value of $\tilde{\mu}_0$ is represented by the decision point $D(\tilde{\mu}_0)$ at the flow diagram (Figure 3). This step shows two possible situations. The first one occurs at margins that are closer to the local isostatic equilibrium. In this case, increasing the value of $\tilde{\mu}_0$ produces remarkable deformations in the estimated model along the entire profile without, however, producing large residuals between the observed and predicted data. On the other hand, at margins presenting large deviations from the local isostatic equilibrium, the deformations produced in the basement and Moho by increasing the value of $\tilde{\mu}_0$ are concentrated at the regions where the margin most deviates from the local isostatic equilibrium. At these regions, there are also large residuals between the observed and predicted data.

Finally, at step 3, try different positive values for σ (equation 23). This parameter controls the deviations of the interpretation model from the isostatic equilibrium at regions presenting large residuals. Small values produce estimated models close to that obtained at step 1. On the other hand, large values produce estimated models close to that obtained at step 2. This parameter must be set as the largest positive number producing (1) a good data fit along the entire profile and (2) an estimated model different from those obtained at steps 1 and 2. This acceptability criterion to define the value of σ is represented by the decision point $D(\sigma)$ at the flow diagram (Figure 3). A good practice is to generate a set of estimates using different values for σ .

APPLICATIONS TO SYNTHETIC DATA

We have simulated a continental margin formed by four layers: water, sediments, crust (continental

and oceanic), and mantle. The geometry of this model is based on a seismic profile crossing the East Greenland margin, over the Jameson Land basin (Peron-Pinvidic et al., 2013), and it shows an extreme crustal thinning. The parameters defining this model are shown in Table 1. The density values of our model are compatible with those commonly used in the literature (e.g., Gradmann et al., 2017). By following the algorithm described in the previous section, we inverted the simulated gravity disturbance produced by our synthetic margin.

We start with the intermediate model \mathbf{p}' (not shown) obtained at step 1 (Figure 3) using only the equality constraints with parameters $\tilde{\mu}_3 = 10^1$ and $\tilde{\mu}_4 = 10^2$. The remaining parameters $\tilde{\mu}_0$, $\tilde{\mu}_1$, and $\tilde{\mu}_2$ are equal to zero. The interpretation model was defined using the parameters shown in Table 1. We assumed $S_0 = 48$ km and chose an initial approximation for ΔS equal to 7 km, which corresponds to a reference Moho deeper than the true one (Table 1). The intermediate model \mathbf{p}' (not shown) contains pinnacles around the a priori

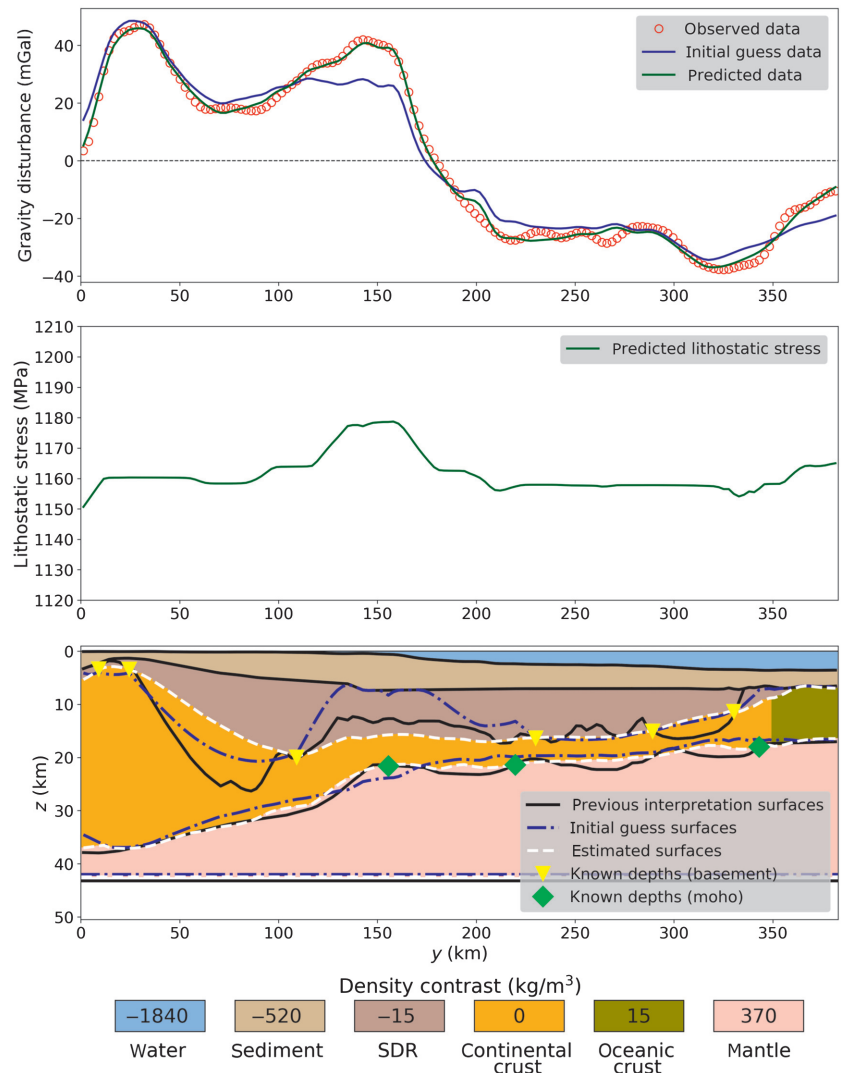


Figure 15. Application to real data from the Pelotas Basin, Brazil. Estimated model $\mathbf{p}^{(3)}$ obtained at the end of step 3 (Figure 3) using $\mathbf{p}^{(2)}$ (Figure 14) as the initial approximation (the dashed blue lines) and $\sigma = 7$ (equation 23). The remaining information is the same as that shown in the caption of Figure 13.

information at the basement and Moho. Despite the good data fit, it does not retrieve the true geometries of the basement and Moho.

Figure 4 shows the estimated model $\mathbf{p}^{(1)}$ obtained at the end of step 1 (Figure 3) with $\tilde{\mu}_1 = 10^1$ and $\tilde{\mu}_2 = 10^2$. Using these values, the method was able to remove the pinnacles of the intermediate model (not shown). Note that not only the initial approximation for the reference Moho but also those for the basement and Moho surfaces (the dashed blue lines) are different from the true model (the continuous black lines). As we can see, the estimated Moho and reference Moho are very close to the true ones. On the other hand, the estimated basement is smooth and presents large differences (≈ 5 km) relative to the true one at the region between 100 and 150 km, where the model shows a pronounced crustal thinning. Despite these large differences, the predicted gravity disturbance and lithostatic stress are very close to the simulated values. By analyzing the predicted lithostatic stress curve, we can see that the model can be considered in local isostatic equilibrium at the regions located

before 75 km and after 250 km. As we can see, the region located between 75 and 250 km shows large variations in the basement and Moho surfaces and also the largest deviations from the local isostatic equilibrium.

Figure 5 shows the estimated model $\mathbf{p}^{(2)}$ obtained at the end of step 2 (Figure 3), using $\tilde{\mu}_0 = 10^3$ (equation 22). In comparison to the estimated model $\mathbf{p}^{(1)}$ (Figure 4), this model shows a smooth lithostatic stress curve as a consequence of the isostatic constraint. This constraint has produced little effect on the estimated reference Moho, resulted in a relatively worse estimated Moho, and also produced large residuals at the region between 75 and 250 km. On the other hand, it reduced the large differences between the estimated and true basement surfaces. The main improvement occurs at the region between 100 and 150 km, where the true model exhibits pronounced crustal thinning. Note that the isostatic constraint produced little effect at the regions where the model is close to the local isostatic equilibrium (before 75 km and after 250 km).

Figures 6, 7, and 8 show estimated models $\mathbf{p}^{(3)}$ obtained at step 3 (Figure 3) using different values for the parameter σ (equation 23). By comparing with the estimated model $\mathbf{p}^{(2)}$ (Figure 5), the new models show better data fits and improved estimates for the Moho. The main differences are concentrated at the regions coinciding with large residuals and large variations in the lithostatic stress curve shown in Figure 5.

The estimated model obtained with the smallest σ (Figure 6) is close to that obtained at step 1 (Figure 4). In this case, the predicted lithostatic stress curve shows large variations, and the estimated model is far from the isostatic equilibrium. On the other hand, the estimated model obtained with the largest σ (Figure 8) is closer to that obtained at step 2 (Figure 5). In this case, the predicted lithostatic stress curve is smoother than that obtained with $\sigma = 1$ (Figure 6). In comparison to these two models, that shown in Figure 7 exhibits an intermediate isostatic equilibrium. Despite these differences, all of them produce a very good data fit along the entire profile, as well as having estimated Moho and reference Moho very close to the true ones. It is important to stress that the most significant variations produced by the isostatic constraint in the estimated basement and Moho are concentrated at the central part of the profile, where the model presents large deviations from the isostatic equilibrium.

These results obtained with different σ values (equation 23) show that the isostatic constraint is not able to completely remove the ambiguity of the inverse problem. Instead they show that, by properly combining isostasy and a priori information, our method is able to produce a set of estimated models exhibiting different amounts of isostatic equilibrium, but practically the same data fit. The differences are concentrated at the central part of the profile, where the true lithostatic curve contains large variations. At the extremities, these models are very similar to each other, the

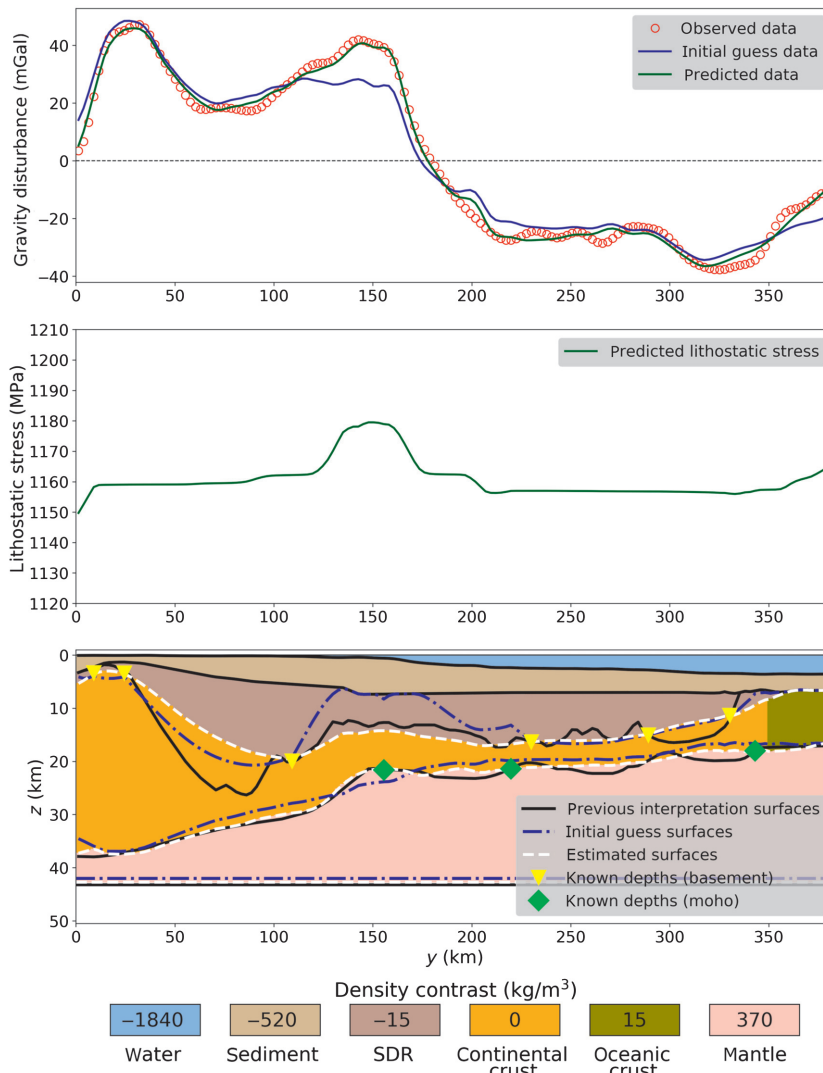


Figure 16. Application to real data from the Pelotas Basin, Brazil. Estimated model $\mathbf{p}^{(3)}$ obtained at the end of step 3 (Figure 3) using $\mathbf{p}^{(2)}$ (Figure 14) as the initial approximation (the dashed blue lines) and $\sigma = 17.6$ (equation 23). The remaining information is the same as that shown in the caption of Figure 13.

lithostatic curves are almost flat, and the models are close to the isostatic equilibrium.

The results obtained with the model based on the East Greenland margin illustrate the case in which our method is applied to a margin presenting large deviations from the local isostatic equilibrium. Figures 9, 10, and 11 show results obtained with a simple model (Table 2) that contains small variations in the lithostatic stress curve and can be considered in local isostatic equilibrium along the entire profile, except at the COT, located at $y_{COT} = 170$. As we can see, the result obtained at step 1 (Figure 9), without the isostatic constraint, is very good and shows the estimated basement and Moho being very close to the true ones. Figure 10 shows that, using the isostatic constraint, the estimated model is better than that obtained at step 1, but the differences are small. Note that differently for the result obtained with the model based on the East Greenland margin (Figure 5), the use of the isostatic constraint does not produce large residuals between the observed and predicted data. This is also the case for the result obtained by increasing the importance of the isostatic constraint (Figure 11). In this case, however, we can see that the isostatic constraint produced a very poor estimated model. The absence of large residuals between the observed and predicted data indicates that the model can be considered in local isostatic equilibrium along the whole profile.

We have also prepared additional tests (in the form of supplementary material that can be accessed through the following links: S1.pdf, S2.pdf, and S3.pdf) for investigating the (1) robustness of our method to the initial approximations used in the nonlinear inversion, (2) the sensitivity of our method to different combinations of constraints, and the (3) quantity of a priori information used at the basement and Moho. Our results show that, even by using initial approximations very different from each other and from the true models, our method produces almost the same result at step 2 and, consequently, at step 3 of our algorithm. They also show that the proposed constraints are not able to retrieve the true basement and Moho if used individually. Instead, the additional results show that our method is able to produce estimated models close to the true one by properly combining all the constraints. Finally, they show that our method is not strongly dependent on the quantity of a priori information at the basement and Moho. This is an important issue because, in real-world situations, it can be very difficult to obtain such control points.

APPLICATION TO FIELD DATA

We applied our method to invert gravity disturbance data on a profile located over the Pelotas Basin (Stica et al., 2014), southern of Brazil (Figure 12). This basin is considered a classic example of volcanic margin (Geoffroy, 2005). The gravity disturbance data are provided by the combined global gravity field model EIGEN-6C4

(Förste et al., 2014), one of the latest releases of the European Improved Gravity Model of the Earth by New Techniques series. We have used data fromETOPO-1 to constrain the bathymetry along the profile (Amante and Eakins, 2009). In addition, we have used a priori information about the basement and Moho depths obtained from the seismic interpretations presented by Stica et al. (2014) and Zalán (2015) to define the equality constraints (equations 20 and 21) and the initial approximation used in the nonlinear inversion.

Figures 13 and 14 show the estimated models obtained at steps 1 and 2, respectively. Parameters defining the interpretation model are shown in Table 3. As we can see, the estimated model obtained at step 2 produces a good data fit along the whole profile, except at region ≈ 150 km. Figures 15, 16, and 17 show the estimated models obtained at step 3 using different values for parameter σ (equation 23). Different from the model obtained at step 2 (Figure 14), the new models show very good data fits along the entire profile.

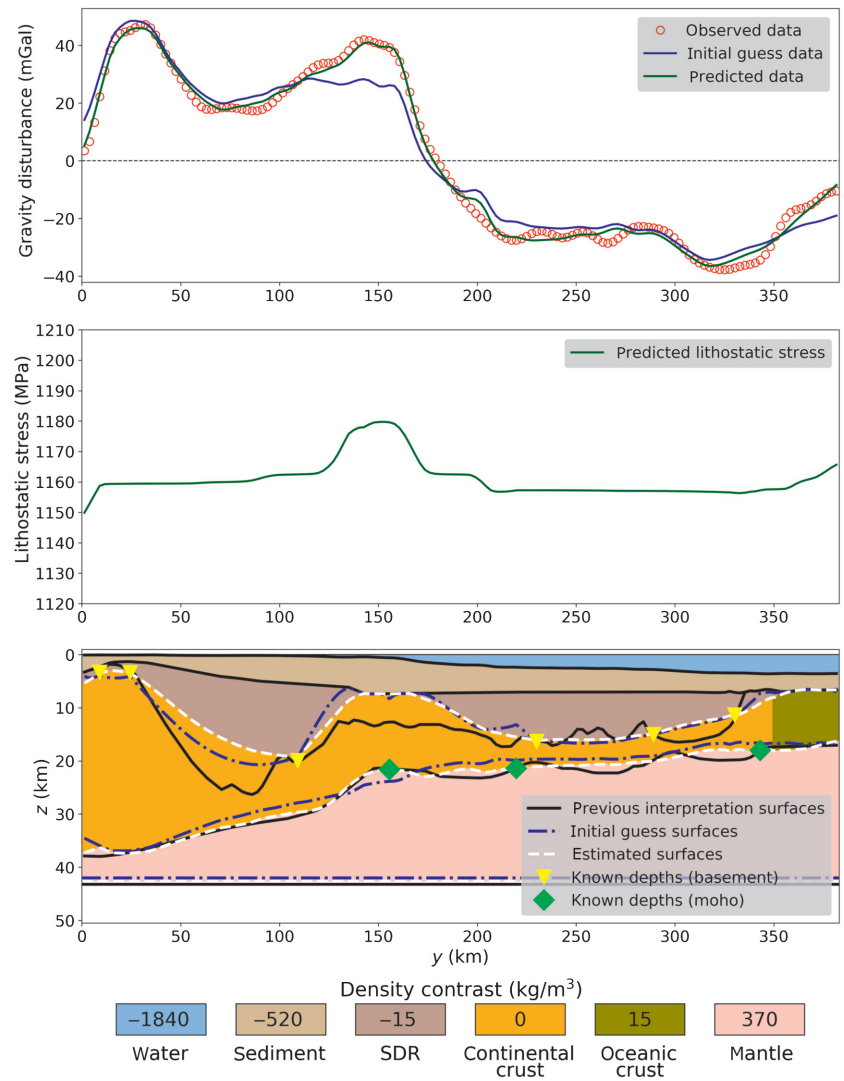


Figure 17. Application to real data from the Pelotas Basin, Brazil. Estimated model $p^{(3)}$ obtained at the end of step 3 (Figure 3) using $p^{(2)}$ (Figure 14) as the initial approximation (the dashed blue lines) and $\sigma = 19$ (equation 23). The remaining information is the same as that shown in the caption of Figure 13.

The estimated lithostatic stress curves produced by these models show abrupt variations close to 150 km and are practically flat in the remaining parts of the profile. These results suggest that the margin is mostly in isostatic equilibrium, except at the region ≈ 150 km. Figure 18 shows an alternative model obtained at step 3. In this model, the parameter σ (equation 23) and the density values in layer 2 (sediment + SDR) are different from those used to obtain the models shown in Figures 15–17.

The estimated models shown in Figures 16 and 18 are close to those proposed by Stica et al. (2014) and Zalán (2015) (the continuous black lines). The larger differences (≈ 10 km) occur at the basement, along the first 100 km of the profile. At this region, Zalán (2015) proposes a steep variation in the basement relief, which shows a maximum depth ≈ 30 km. These differences may be associated to the data we used to obtain our model. We used satellite

gravity data, whereas Stica et al. (2014) and Zalán (2015) use gravity, magnetic, and seismic sections available to the petroleum industry. These differences may also be associated to lateral density variations that had not been included in our model, located in the sediment, SDR, crust, or mantle. Alternatively, they might represent underplated mafic to ultramafic magma at the base of the crust, which would represent positive anomalous masses and produce a gravity high. To compensate this high, the inversion would estimate a deeper basement, which would be closer to Zalán's model. We do not attempt to propose a new model for the Pelotas Basin, but we show how simple isostatic considerations can be combined with a priori information to explore the range of acceptable models.

CONCLUSION

We present a gravity inversion method for simultaneously estimating the geometries of the basement and Moho, as well as the constant depth of the reference Moho on a profile crossing a passive rifted margin. The method is formulated as a nonlinear inverse problem by imposing local isostatic equilibrium. There are four main differences between our method and those in the literature. The first is that at each iteration of the nonlinear inversion, our method estimates corrections for the geometries of basement and Moho simultaneously. It means that we do not estimate the Moho, use it to compute a residual gravity anomaly, and then invert these residual data to obtain the basement. Another difference is that we do not use local isostasy to directly link the geometries of basement and Moho. Rather, we impose smoothness on the lithostatic stress exerted by the interpretation model on a constant compensation depth, below which there are no lateral density variations. Our method also varies the weight of the isostatic constraint along the profile, which is particularly useful for delimiting regions that deviate from the isostatic equilibrium. Finally, our method also differs from those in the literature because it attempts to use isostasy for exploring (and not necessarily reducing) the inherent ambiguity of gravity methods.

Tests with synthetic data produced by a realistic model based on the East Greenland margin show that our method can be used to successfully delimit regions conforming to and deviating from the local isostatic equilibrium, as well as to generate a set of possible solutions that have different degrees of isostatic equilibrium and produce equally good data fits. The interpreter must choose the best estimated model based on the available a priori information and their knowledge about the study area. Besides these results show that the isostatic constraint can improve the estimated models at rifted margins showing pronounced crustal thinning. The large variations in the basement and Moho reliefs at these margins induce large variations in the lithostatic stress.

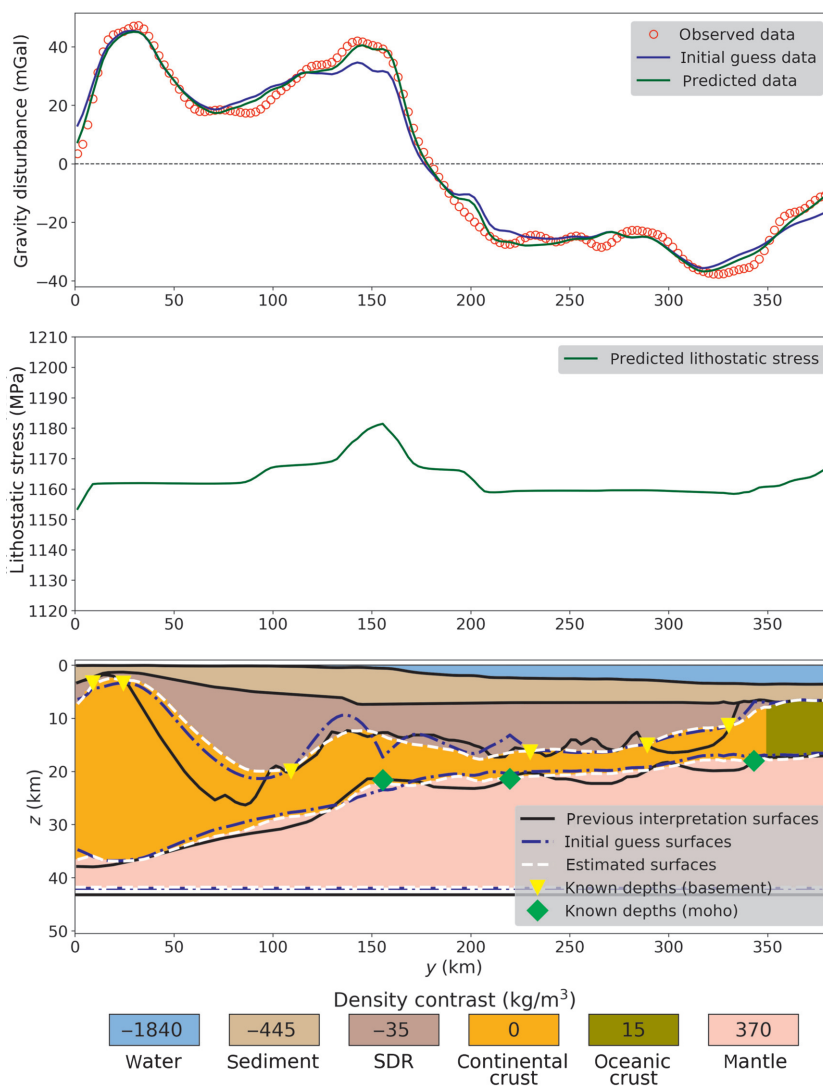


Figure 18. Application to real data from the Pelotas Basin, Brazil. Alternative estimated model $\mathbf{p}^{(3)}$ obtained at the end of step 3 (Figure 3). The differences between this model and those shown in Figures 15, 16, and 17 are the densities $\rho^{(1)}$ and $\rho^{(2)}$ attributed to the sediments and SDR (Table 3), as well as parameter σ (equation 23). In this alternative model, $\rho^{(1)} = 2425 \text{ kg/m}^3$, $\rho^{(2)} = 2835 \text{ kg/m}^3$, and $\sigma = 17$. The remaining information is the same as that shown in the caption of Figure 13.

This is a good scenario for using our isostatic constraint to explore different models. We also present results obtained with a simple model simulating a margin close to the local isostatic equilibrium along the entire profile. The basement and Moho surfaces in this simple model are relatively smooth. As a consequence, the isostatic constraint does not improve the estimated model significantly if compared with that obtained using the smoothness constraint. Applications to field data over the Pelotas Basin, considered a classic volcanic margin at the southern of Brazil, produced results in agreement with a previous interpretation obtained independently. Our results also delimit regions that can and cannot be considered in local isostatic equilibrium along the profile.

The problem of simultaneously estimating the geometries of the basement and Moho surfaces is very ambiguous, and some simplifications must be made. One of these simplifications consists of considering bulk density values for each column forming the continental and oceanic crusts. The interpreter must predefine the function describing the horizontal density variation of the crust along the profile, including the region close to the COT. In most practical situations, however, the interpreter will not have access to a detailed description of the density variations within the crust, and a regional approximation will have to be used instead. As a consequence, local errors in the estimated basement and Moho surfaces are expected at regions presenting local density variations in the deeper parts of the continental crust and in the oceanic crust. Another limitation of our method is that it requires a priori information about the upper layers located below the water layer. This information can be obtained, for example, from seismic data and can be used to set the densities of the layers located right below the ocean bottom. If no a priori information is available at the study area, the interpreter will have to use approximated values and test different models. Errors in this approximation may negatively impact the estimated model, especially in the basement surface. Further research could be conducted to generalize our method to estimate 3D models, including lateral density variations in the upper mantle and depth-dependent density distributions at the layers representing sediments.

ACKNOWLEDGMENTS

The authors are grateful to the editors E. Gasperikova, J. Shragge, and X. Li; reviewers J. G. Abdeslem and Bob Ferderer; and the anonymous reviewers for their constructive comments and suggestions. We are deeply indebted to the open-source Python toolkit for geophysical modeling and inversion Fatiando a Terra (Uieda et al., 2013), the open-source libraries Numpy/Scipy (Virtanen et al., 2001) for array-based computations, matplotlib (Hunter, 2007) for plotting, and also Jupyter Notebook (<https://jupyter.org/>) for putting it all together. V. C. Oliveira Jr., was supported by fellowships from the Brazilian research agencies CNPq (grant no. 308945/2017-4) and FAPERJ (grant no. E-26/202.729/2018).

DATA AND MATERIALS AVAILABILITY

Data associated with this research are available and can be obtained by contacting the corresponding author.

REFERENCES

- Amante, C., and B. W. Eakins, 2009, ETOPO1 1 arc-minute global relief model — Procedures, data sources and analysis: NOAA Technical Memo-
randum NESDIS NGDC-24, National Geophysical Data Center, NOAA (online; accessed 2019-10-03).
- Aster, R. C., B. Borchers, and C. H. Thurber, 2005, Parameter estimation and inverse problems: Academic Press, International Geophysics.
- Bagherbandi, M., and M. Eshagh, 2012, Crustal thickness recovery using an isostatic model and GOCE data: *Earth, Planets and Space*, **64**, 1053–1057, doi: [10.5047/eps.2012.04.009](https://doi.org/10.5047/eps.2012.04.009).
- Barbosa, V. C. F., J. B. C. Silva, and W. E. Medeiros, 1997, Gravity inversion of basement relief using approximate equality constraints on depths: *Geophysics*, **62**, 1745–1757, doi: [10.1190/1.1444275](https://doi.org/10.1190/1.1444275).
- Barbosa, V. C. F., J. B. C. Silva, and W. E. Medeiros, 1999a, Gravity inversion of a discontinuous relief stabilized by weighted smoothness constraints on depth: *Geophysics*, **64**, 1429–1437, doi: [10.1190/1.1444647](https://doi.org/10.1190/1.1444647).
- Barbosa, V. C. F., J. B. C. Silva, and W. E. Medeiros, 1999b, Stable inversion of gravity anomalies of sedimentary basins with non-smooth basement reliefs and arbitrary density contrast variations: *Geophysics*, **64**, 754–764, doi: [10.1190/1.1444585](https://doi.org/10.1190/1.1444585).
- Barnes, G., and J. Barraud, 2012, Imaging geologic surfaces by inverting gravity gradient data with depth horizons: *Geophysics*, **77**, no. 1, G1–G11, doi: [10.1190/geo2011-0149.1](https://doi.org/10.1190/geo2011-0149.1).
- Barzaghi, R., and L. Biagi, 2014, The collocation approach to Moho estimate: *Annals of Geophysics*, **57**, S0190, doi: [10.4401/ag-6367](https://doi.org/10.4401/ag-6367).
- Bott, M. H. P., 1960, The use of rapid digital computing methods for direct gravity interpretation of sedimentary basins: *Geophysical Journal International*, **3**, 63–67, doi: [10.1111/j.1365-246X.1960.tb00065.x](https://doi.org/10.1111/j.1365-246X.1960.tb00065.x).
- Braatenberg, C., E. Pagot, Y. Wang, and J. Fang, 2003, Bathymetry and crustal thickness variations from gravity inversion and flexural isostasy in C. Hwang, C. K. Shum, and J. Li, eds., *Satellite altimetry for geodesy, geophysics and oceanography*: Springer Berlin Heidelberg, 143–149.
- Braatenberg, C., F. Pettenati, and M. Zadro, 1997, Spectral and classical methods in the evaluation of Moho undulations from gravity data: The NE Italian Alps and isostasy: *Journal of Geodynamics*, **23**, 5–22, doi: [10.1016/S0264-3707\(96\)00024-5](https://doi.org/10.1016/S0264-3707(96)00024-5).
- Braatenberg, C., and M. Zadro, 1999, Iterative 3D gravity inversion with integration of seismologic data: *Bollettino di Geofisica Teorica ed Applicata*, **40**, 469–475.
- Camacho, A. G., J. Fernández, and J. Gottsmann, 2011, A new gravity inversion method for multiple subhorizontal discontinuity interfaces and shallow basins: *Journal of Geophysical Research: Solid Earth*, **116**, B02413, doi: [10.1029/2010JB008023](https://doi.org/10.1029/2010JB008023).
- Chakravarthi, V., and N. Sundararajan, 2007, 3D gravity inversion of basement relief — A depth-dependent density approach: *Geophysics*, **72**, no. 2, I23–I32, doi: [10.1190/1.2431634](https://doi.org/10.1190/1.2431634).
- Condi, F. J., C. A. Zelt, D. S. Sawyer, and G. J. Hirasaki, 1999, Gravity inversion for rifted margin deep structure using extension and isostatic constraints: *Geophysical Journal International*, **138**, 435–446, doi: [10.1046/j.1365-246X.1999.00872.x](https://doi.org/10.1046/j.1365-246X.1999.00872.x).
- Cordell, L., and R. G. Henderson, 1968, Iterative three-dimensional solution of gravity anomaly data using a digital computer: *Geophysics*, **33**, 596–601, doi: [10.1190/1.1439955](https://doi.org/10.1190/1.1439955).
- Fairhead, J. D., C. M. Green, and D. Blitzkow, 2003, The use of GPS in gravity surveys: *The Leading Edge*, **22**, 954–959, doi: [10.1190/1.1623636](https://doi.org/10.1190/1.1623636).
- Ferderer, R., J. Mariano, and J. Shoffner, 2017, Inversion of gravity data using general local isostasy: 87th Annual International Meeting, SEG, Expanded Abstracts, 1718–1722, doi: [10.1190/segam2017-17676109.1](https://doi.org/10.1190/segam2017-17676109.1).
- Förste, C., S. Bruinsma, O. Abrilovos, J.-M. Lemoine, J. C. Marty, F. Flechtner, G. Balmino, F. Barthelmes, and R. Biancale, 2014, EIGEN-6C4 The latest combined global gravity field model including GOCE data up to degree and order 2190 of GFZ Potsdam and GRGS Toulouse: GFZ Data Services, doi: [10.5880/icgem.2015.1](https://doi.org/10.5880/icgem.2015.1).
- García-Abdeslem, J., 2017, Nonlinear inversion of isostatic residual gravity data from Montage Basin, northern Gulf of California: *Geophysics*, **82**, no. 3, G45–G55, doi: [10.1190/geo2016-0144.1](https://doi.org/10.1190/geo2016-0144.1).
- Geoffroy, L., 2005, Volcanic passive margins: *Comptes Rendus Geoscience*, **337**, 1395–1408, doi: [10.1016/j.cret.2005.10.006](https://doi.org/10.1016/j.cret.2005.10.006).
- Graddmann, S., C. Haase, and J. Ebbing, 2017, Isostasy as a tool to validate interpretations of regional geophysical datasets — Application to the mid-Norwegian continental margin: *Geological Society, London, Special Publications* **447**, 279–297.
- Granster, H., 1987, Three-dimensional interpretation of gravity data from sedimentary basins using an exponential density-depth function: *Geophysical Prospecting*, **35**, 1030–1041, doi: [10.1111/j.1365-2478.1987.tb00858.x](https://doi.org/10.1111/j.1365-2478.1987.tb00858.x).
- Guspi, F., 1993, Noniterative nonlinear gravity inversion: *Geophysics*, **58**, 935–940, doi: [10.1190/1.1443484](https://doi.org/10.1190/1.1443484).
- Hackney, R. I., and W. E. Featherstone, 2003, Geodetic versus geophysical perspectives of the gravity anomaly: *Geophysical Journal International*, **154**, 35–43, doi: [10.1046/j.1365-246X.2003.01941.x](https://doi.org/10.1046/j.1365-246X.2003.01941.x).
- Heiskanen, W. A., and H. Moritz, 1967, Physical geodesy: W.H. Freeman and Company.
- Hinze, W. J., C. Aiken, J. Brozena, B. Coakley, D. Dater, G. Flanagan, R. Forsberg, T. Hildenbrand, G. R. Keller, J. Kellogg, R. Kucks, X. Li, A.

- Mainville, R., Morin, M., Pilkington, D., Plouff, D., Ravat, D., Roman, J., Urrutia-Fucugauchi, M., Véronneau, M., Webring, and D. Winchester, 2005, New standards for reducing gravity data: The North American gravity database: *Geophysics*, **70**, no. 4, J25–J32, doi: [10.1190/1.1988183](https://doi.org/10.1190/1.1988183).
- Hunter, J. D., 2007, Matplotlib: A 2D graphics environment: *Computing in Science & Engineering*, **9**, 90–95, doi: [10.1109/MCSE.2007.55](https://doi.org/10.1109/MCSE.2007.55).
- Li, X., and H.-J. Götsche, 2001, Ellipsoid, geoid, gravity, geodesy, and geophysics: *Geophysics*, **66**, 1660–1668, doi: [10.1190/1.1487109](https://doi.org/10.1190/1.1487109).
- Lima, W. A., C. M. Martins, J. B. Silva, and V. C. Barbosa, 2011, Total variation regularization for depth-to-basement estimate — Part 2: Physico-geologic meaning and comparisons with previous inversion methods: *Geophysics*, **76**, no. 1, I13–I20, doi: [10.1190/1.3524547](https://doi.org/10.1190/1.3524547).
- Martins, C. M., V. C. Barbosa, and J. B. Silva, 2010, Simultaneous 3D depth-to-basement and density-contrast estimates using gravity data and depth control at few points: *Geophysics*, **75**, no. 3, I21–I28, doi: [10.1190/1.3380225](https://doi.org/10.1190/1.3380225).
- Martins, C. M., W. A. Lima, V. C. Barbosa, and J. B. Silva, 2011, Total variation regularization for depth-to-basement estimate — Part 1: Mathematical details and applications: *Geophysics*, **76**, no. 1, I1–I12, doi: [10.1190/1.3524286](https://doi.org/10.1190/1.3524286).
- Nagy, D., G. Papp, and J. Benedek, 2000, The gravitational potential and its derivatives for the prism: *Journal of Geodesy*, **74**, 552–560, doi: [10.1007/s001900000116](https://doi.org/10.1007/s001900000116).
- Oldenburg, D. W., 1974, The inversion and interpretation of gravity anomalies: *Geophysics*, **39**, 526–536, doi: [10.1190/1.1440444](https://doi.org/10.1190/1.1440444).
- Peron-Pinvidic, G., G. Manatschal, and P. T. Osmundsen, 2013, Structural comparison of archetypal Atlantic rifted margins: A review of observations and concepts: *Marine and Petroleum Geology*, **43**, 21–47, doi: [10.1016/j.marpetgeo.2013.02.002](https://doi.org/10.1016/j.marpetgeo.2013.02.002).
- Reamer, S. K., and J. F. Ferguson, 1989, Regularized two-dimensional Fourier gravity inversion method with application to the Silent Canyon Caldera, Nevada: *Geophysics*, **54**, 486–496, doi: [10.1190/1.1442675](https://doi.org/10.1190/1.1442675).
- Roy, A., 1962, Ambiguity in geophysical interpretation: *Geophysics*, **27**, 90–99, doi: [10.1190/1.1438985](https://doi.org/10.1190/1.1438985).
- Salem, A., 2017, Gravity modeling a rifted continental margin, WO2017131848, <https://patentscope.wipo.int/search/en/detail.jsf?docId=WO2017131848>, accessed 15 November 2019.
- Salem, A., C. Green, M. Stewart, and D. D. Lerma, 2014, Inversion of gravity data with isostatic constraints: *Geophysics*, **79**, no. 6, A45–A50, doi: [10.1190/geo2014-0220.1](https://doi.org/10.1190/geo2014-0220.1).
- Sampietro, D., 2015, Geological units and Moho depth determination in the Western Balkans exploiting GOCE data: *Geophysical Journal International*, **202**, 1054–1063, doi: [10.1093/gji/ggv212](https://doi.org/10.1093/gji/ggv212).
- Sen, M. K., and P. L. Stoffa, 2013, Global optimization methods in geophysical inversion, 2nd ed.: Cambridge University Press.
- Shin, Y. H., C.-K. Shum, C. Braatenberg, S. M. Lee, H. Xu, K. S. Choi, J. H. Baek, and J. U. Park, 2009, Three-dimensional fold structure of the Tibetan Moho from GRACE gravity data: *Geophysical Research Letters*, **36**, L01302, doi: [10.1029/2008GL036068](https://doi.org/10.1029/2008GL036068).
- Silva, J. B., D. C. Costa, and V. C. Barbosa, 2006, Gravity inversion of basement relief and estimation of density contrast variation with depth: *Geophysics*, **71**, no. 5, J51–J58, doi: [10.1190/1.2236383](https://doi.org/10.1190/1.2236383).
- Silva, J. B. C., W. E. Medeiros, and V. C. F. Barbosa, 2001, Pitfalls in nonlinear inversion: *Pure and Applied Geophysics*, **158**, 945–964, doi: [10.1007/PL00001215](https://doi.org/10.1007/PL00001215).
- Silva, J. B., A. S. Oliveira, and V. C. Barbosa, 2010, Gravity inversion of 2D basement relief using entropic regularization: *Geophysics*, **75**, no. 3, I29–I35, doi: [10.1190/1.3374358](https://doi.org/10.1190/1.3374358).
- Silva, J. B. C., and D. F. Santos, 2017, Efficient gravity inversion of basement relief using a versatile modeling algorithm: *Geophysics*, **82**, no. 2, G23–G34, doi: [10.1190/geo2015-0627.1](https://doi.org/10.1190/geo2015-0627.1).
- Silva, J. B. C., D. F. Santos, and K. P. Gomes, 2014, Fast gravity inversion of basement relief: *Geophysics*, **79**, no. 5, G79–G91, doi: [10.1190/geo2014-0024.1](https://doi.org/10.1190/geo2014-0024.1).
- Skeels, D. C., 1947, Ambiguity in gravity interpretation: *Geophysics*, **12**, 43–56, doi: [10.1190/1.1437295](https://doi.org/10.1190/1.1437295).
- Stica, J. M., P. V. Zalán, and A. L. Ferrari, 2014, The evolution of rifting on the volcanic margin of the Pelotas Basin and the contextualization of the Paraná-Etendeka LIP in the separation of Gondwana in the South Atlantic: *Marine and Petroleum Geology*, **50**, 1–21, doi: [10.1016/j.marpetgeo.2013.10.015](https://doi.org/10.1016/j.marpetgeo.2013.10.015).
- Tanner, J. G., 1967, An automated method of gravity interpretation: *Geophysical Journal of the Royal Astronomical Society*, **13**, 339–347, doi: [10.1111/j.1365-246X.1967.tb02164.x](https://doi.org/10.1111/j.1365-246X.1967.tb02164.x).
- Turcotte, D. L., and G. Schubert, 2002, *Geodynamics*, 2nd ed.: Cambridge University Press.
- Uieda, L., and V. C. Barbosa, 2017, Fast nonlinear gravity inversion in spherical coordinates with application to the South American Moho: *Geophysical Journal International*, **208**, 162–176, doi: [10.1093/gji/ggw390](https://doi.org/10.1093/gji/ggw390).
- Uieda, L., V. C. Oliveira Jr., and V. C. F. Barbosa, 2013, Modeling the earth with Fatiando a Terra: Proceedings of the 12th Python in Science Conference, 96–103.
- Vajda, P., P. Vaníček, and B. Meurers, 2006, A new physical foundation for anomalous gravity: *Studia Geophysica et Geodaetica*, **50**, 189–216, doi: [10.1007/s11200-006-0012-1](https://doi.org/10.1007/s11200-006-0012-1).
- Vajda, P., P. Vaníček, P. Novák, R. Tenzer, and A. Ellmann, 2007, Secondary indirect effects in gravity anomaly data inversion or interpretation: *Journal of Geophysical Research: Solid Earth*, **112**, B06411, doi: [10.1029/2006JB004470](https://doi.org/10.1029/2006JB004470).
- van der Meijde, M., J. Julià, and M. Assumpção, 2013, Gravity derived Moho for South America: *Tectonophysics*, **609**, 456–467, doi: [10.1016/j.tecto.2013.03.023](https://doi.org/10.1016/j.tecto.2013.03.023).
- Virtanen, P., R. Gommers, T. E. Oliphant, M. Haberland, T. Reddy, D. Cournapeau, E. Burovski, P. Peterson, W. Weckesser, J. Bright, M. K. van der Walt, M. Brett, J. Wilson, G. Jarrod, N. Mayorov, R. J. Nelson, E. Jones, R. Kern, E. Larson, C. J. Carey, I. Polat, Y. Feng, E. W. Moore, J. Plouff, D. Laxalde, J. Perktold, R. Cimrman, I. Henriksen, E. A. Quintero, C. R. Harris, A. M. Archibald, A. H. Ribeiro, F. Pedregosa, and P. van Mulbregt, 2021, SciPy: Open source scientific tools for Python, <http://www.scipy.org/>, accessed 10 March 2019.
- Zalán, P. V., 2015, Similarities and differences between magma-poor and volcanic passive margins applications to the Brazilian marginal basins: 14th International Congress of the Brazilian Geophysical Society & EXPOGEF, 37–42.